Geomorphic Evolution of the Nushki Segment of the Chaman Fault in Western Pakistan

……...

A Thesis

Presented to

the Faculty of the Department of Earth and Atmospheric Sciences

University of Houston

……

In Partial Fulfillment

of the Requirements for the Degree

Master of Science

……

By

Yahaya Abubakar

December, 2012

Geomorphic Evolution of the Nushki Segment of the Chaman Fault in Western Pakistan

_____

Yahaya Abubakar

APPROVED BY:

_____

Dr. Shuhab D. Khan, Associate Professor
(Committee Chair)
Department of Earth and Atmospheric Sciences
University of Houston

_____

Dr. Jolante van Wijk, Assistant Professor
Department of Earth and Atmospheric Sciences
University of Houston

_____

Dr. Lewis A. Owen, Professor
Department of Geology
University of Cincinnati, Ohio

_____

Dr. Mark A. Smith, Dean,
College of Natural Sciences and Mathematics
University of Houston

Dedication

This work is dedicated to my father; the Late Alhaji Sule Abu and my mother, Mrs. Elizabeth Abu who have stood by me and offered invaluable moral and financial support all through my life.

Acknowledgements

The journey so far has been one of great challenges and rewards which would not have been possible without the support, guidance, and motivation from a whole lot of people. My hearty thanks and appreciation goes to my amiable advisor, Dr. Shuhab Khan, whose kind disposition and invaluable guidance immensely helped in the completion of this work.

My appreciation also goes to the other members of my thesis committee; Dr. Lewis Owen and Dr. Jolante VanWijk for taking out time to read through this work and offering very useful suggestions. Dr. Lewis Owen greatly assisted by allowing me unrestricted access to the cosmogenic laboratory at the University of Cincinnati for geochemical analysis. Special thanks to Kate Hedrich and Sarah Trischer of the Geology department, University of Cincinnati for their assistance with the geochemical analysis.

My hearty thanks also go to my hosts in Cincinnati; Alan Santistevan and Youseff Hussein for their hospitality during my stay there.

Special mention must also be made of members of the GeoRS research group at the University of Houston; Ismail Abir, Kevin Schmidt, Xu Han, Kivanc Biber, Ayca Karacay, Unal, John Epps, Jessica Quintannar, Shams Ul-Hadi, Maisam Otoum, and Zheng Huang for all their support. Shams Ul-Hadi was especially helpful in collecting samples from the study area and lectured me extensively on the tectonic history of the study area, I remain eternally grateful for his assistance.

The support of members of my immediate family is highly appreciated; especially my brother Mr. Victor Abu and his wife, Dr. Eme Amba Abu who both made my early transition in the United States hitch free.

Finally my entire graduate education would not be possible without the world renowned faculty of the Earth and Atmospheric Science department, University of Houston. I say a big thanks to you all for your positive impacts on my academic pursuits. Special thanks to Dr. John Casey for granting me a teaching assistantship which greatly eased the financial burden of paying for graduate school.

Geomorphic Evolution of the Nushki Segment of the Chaman Fault in Western Pakistan

……...

An Abstract of a Thesis

Presented to

the Faculty of the Department of Earth and Atmospheric Sciences

University of Houston

……

In Partial Fulfillment

of the Requirements for the Degree

Master of Science

……

By

Yahaya Abubakar

December 2012

Abstract

The Chaman strike-slip fault marks the western boundary of the collision zone between the Indian and Eurasian plates. It accommodates both lateral translation and convergence of the Indian plate beneath the Eurasian plate and connects the Makran subduction zone to the Himalayan convergence zone. The geomorphic evolution of this very important tectonic feature is relatively unknown compared to other tectonically important faults in the Himalayas such as the Altyn-Tagh and Karakoram faults. The Nushki Basin marks the southern portion of the of the Chaman fault where strike-slip and thrust faults interaction predominates.

This work utilizes a morphometric approach towards understanding the geomorphic evolution of the southern segment of the Chaman fault. Fifteen meter Digital Elevation Models (DEM), Advanced Spaceborne Thermal Emission and Reflection (ASTER), and GeoEye-1 satellite images were all integrated to measure three geomorphic indices; stream-length gradient index (SL), mountain-front sinuosity (Smf), and valley-floor width to height ratio (Vf). Analysis of results obtained from the measured indices shows that evolution of landforms in the area is tectonically controlled with propagation of thrust towards the northern flanks of the basin. This is further supported by the results of topographic analysis carried out on a ridge which shows two wind gaps in the north and a corresponding water gap further south. Measured offsets on Quaternary landforms also vary from the northern to southern flanks of the basin, generally showing a larger total displacement in the northern portion relative to the south.

Table of Contents

List of Figures

List of Tables

List of Abbreviations/Acronyms

ASTER	Advanced Spaceborne Thermal Emission and Reflection Radiometer
DEMs	Digital Elevation Models
Eld	Elevation of left valley divide
EOS	Earth Observation Satellite
Erd	Elevation of right valley divide
ERS	European Remote Sensing satellite
Esc	Elevation of valley floor
ETM	Enhanced Thematic Mapper
E-W	East-West direction
Ga	Wind gap
GIS	Geographic Information System
Gw	Water gap
InSAR	Interferometric Synthetic Aperture Radar
Lmf	Length of mountain front along the foot of the mountain
Ls	Straight line length of mountain front
M	Meters
METI	Ministry of Economy Trade and Industry (Japan)
NASA	National Aeronautics and Space Administration
PGA	Peak Ground Acceleration
RGB	Red-Blue-Green band combination
RPC	Rational Polynomial Coeficient
SCC	Spinatizha Crystalline Complex
SL	Stream-length gradient Index
Smf	Mountain-front sinuosity
SWIR	Short wave infrared

TERRA	A sun synchronous earth observation satellite.
TIR	Thermal Infrared
Vf	Valley-floor width to height ratio.
Vfw	Valley-floor width
VNIR	Very near infrared

CHAPTER 1: INTRODUCTION

Studies of crustal strike-slip faults provide invaluable information for deciphering a whole range of tectonic processes responsible for continental deformation. Research on fault systems such as the Altyn Tagh, Karakoram, and Kunlun in the Himalayas have advanced our understanding of continental deformation into two end-member models of 1) continental extrusion of Eurasia in front of the hard indenter Indian Plate; 2) distributed deformation within the Himalayan-Tibetan orogeny. The Chaman fault system, which defines the western margin of this collision zone, is relatively less studied. Thus, it is pertinent to examine the role of this very important shear system in accommodating crustal shortening of the Himalaya. Recent seismic activity, including the Mw 6.7 Chaman earthquake of 1892 within the shear zone (Ambraseys and Bilham, 2003) place the fault system among a group of recently active faults of the region with a higher deformation rate (Ruleman, et al., 2007). While geologically constrained rates of deformation are in the slip-rate range of 18-39 mm/yr (Lawrence, et al., 1992, Ul-Hadi et al., 2012), the geodetically estimated rates range between 18 mm/yr (Mohadjer, et al., 2010) and 8 mm/yr (Furuya and Satyabala, 2008). Most of these studies were focused in the northern segment of the fault system that runs in western Pakistan (Figures 1.1 and 1.2). This study focuses on the fault, particularly the area around Nushki where strike-slip fault interaction with thrust faults (transpression) becomes more pronounced.

Remote sensing data (ASTER and, GeoEye-1 images) and Digital Elevation Models (DEMs) were integrated to study fault growth and direction of lateral propagation of active strike-slip fault and thrust faults respectively in the Nushki Basin just south of the

Chaman Basin. Geomorphic indices were measured to help in reconstructing the effects of Late Quaternary transpression on landforms in the basin. Careful analysis of the geomorphic indices and topographic analysis on a ridge north of the basin suggest a northward propagation of thrust while varying amounts of displacements were recorded on Quaternary landforms in the basin.

1.1 Geologic Setting

1.1.1 The Chaman Transform Zone

The Chaman fault system is a ~900 km long left lateral transform plate boundary between the Indian and Eurasian plates in Afghanistan and Pakistan

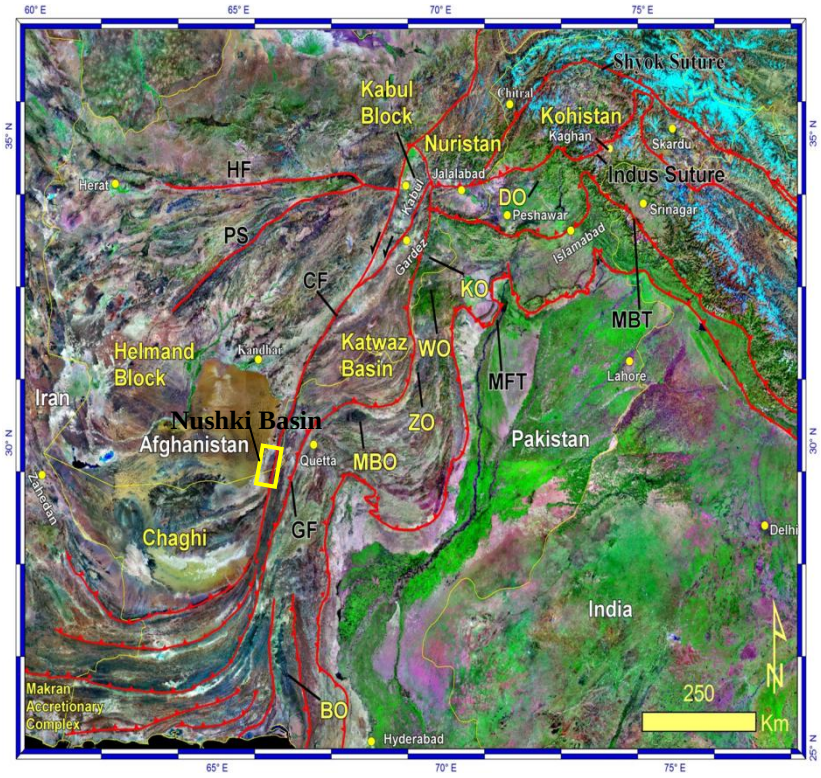

Figure 1.1: Landsat ETM image (Band 7-4-3) of tectonic blocks and active faults around the Himalayas. The Chaman transform zone is on the western boundary of the Indian plate in Pakistan. The Nushki Basin is represented by the yellow box on the southern segment of the Chaman fault. (Modified after Khan and Mahmud, 2009)

(Ruleman et al., 2007; Lawrence et al., 1992). It connects the Makran subduction zone in the south to the Himalayan convergence zone in the north (Figure 1.1). The shear zone is marked by three prominent left-lateral strike-slip faults; namely, the Chaman, Ghazaband, and Ornach-Nal faults. The Chaman fault is the most pronounced active fault that runs along Pakistan's western frontier with Afghanistan from Kalat, in the northern Makran range, pass Quetta and then on to Kabul, Afghanistan with a total of 200 km of left-lateral displacement (Lawrence et al., 1981). According to various studies, the Chaman transform zone first became active in the late Oligocene or early Miocene (Lawrence et al., 1981). The total displacement and slip rate across the Chaman fault system varies in response to the rates of convergence (Lawrence et al., 1981). Oblique convergence occurs near and north of Quetta, where it is accommodated by thrust faulting in ranges to the east of the apparently pure strike-slip Chaman fault (Szeliga et al., 2006).

The Chaman fault system has been seismically active and earthquakes range from moderate to high intensity. The Geological Survey of Pakistan suggests maximum peak ground acceleration (PGA) ranging between 0.24 g to 0.4 g for the region covered by this fault system (Khan, 2008). Several earthquakes ranging in magnitude from 7 to 8.1 have resulted in colossal loss of lives and property in the past. The 1935 Quetta earthquake is one of the examples that took the lives of about 30,000 people and the city was badly damaged. The relative movement between the Indian and Eurasian plate here is at least partially accommodated by aseismic slip along the Chaman fault (Quittmeyer and Kafka, 1984). ERS-1/-2 data indicate a change in range along a 110 km segment of the Chaman

fault by as much as 7.8 mm/yr. The Satellite Radar Interferometry (InSAR) analyses suggest a 110 km segment of the Chaman fault system north of Quetta experiencing shallow aseismic slip. It has been suggested that the plate motion along the Chaman fault is at least accommodated by slow slip episodes following moderate earthquakes in areas around the fault (Furuya and Satyabala, 2007).

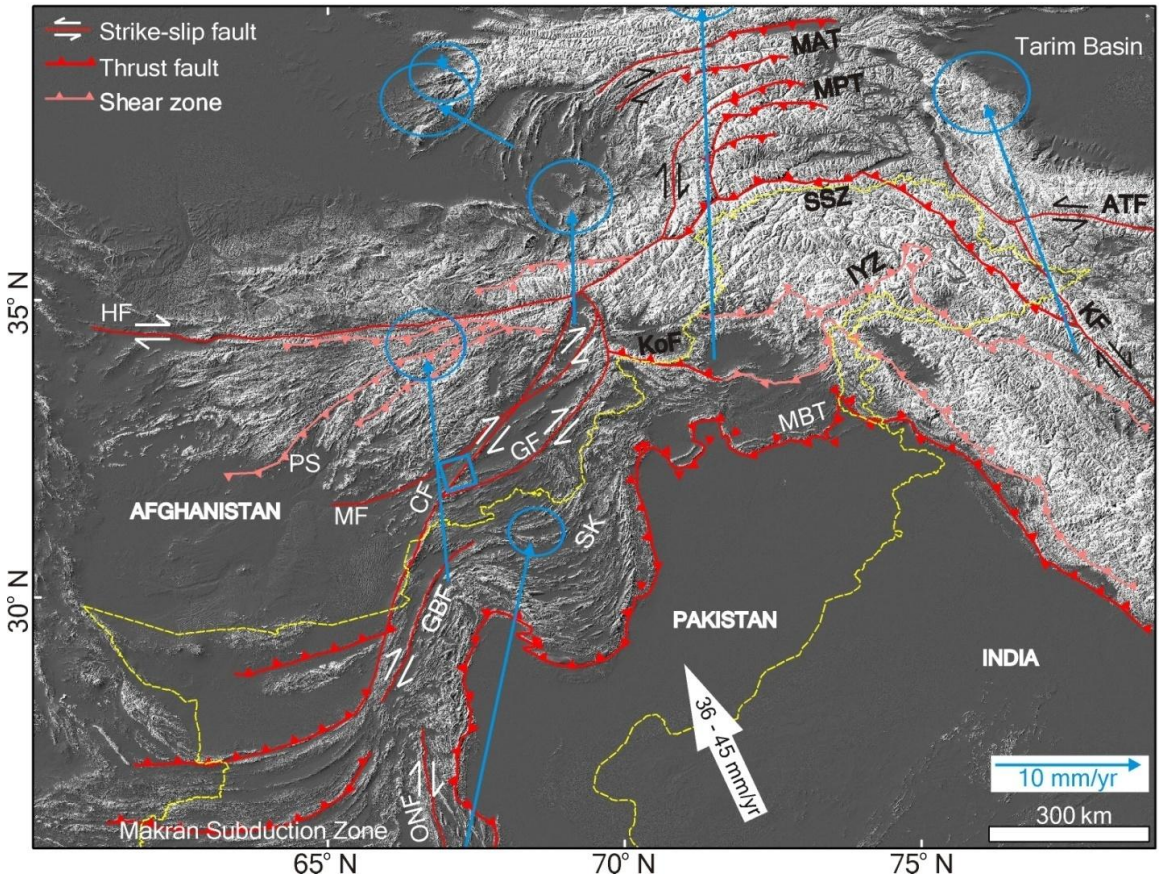

Figure 1.2: Tectonic framework of the northwestern Indian Plate margin and Eurasia. Major active strike-slip faults, thrusts and suture zones (modified after Mohadjer, et al., 2010; Khan et al., 2009, Ul-Hadi, 2012) are displayed on SRTM elevation data. Blue arrows show GPS velocities with respect to fixed Eurasia. The blue box is the position of Synthetic Aperture Radar (SAR) data used in InSAR studies (Furuya and Satyabala, 2008). ATF: Altyn Tagh Fault; GF: Gardiz Fault; HF: Herat Fault; IYS: Indus Yalu Suture Zone; KF: Karakoram Fault; KoF: Konar Fault; MAT: Main Alai Thrust; MBT: Main Boundary Thrust; MF: Mokur Fault; MPT: Main Pamir Thrust; ONF: Ornach-Nal Fault; PS: Panjao shear; SK: Suliman-Kirthar Fold-thrust Belt; SSZ: Shyok Suture Zone. (From Ul-Hadi, 2012)

1.1.2 The Convergence Zones

There are three main zones of convergence interacting with the Chaman transform zone; the Himalayan convergence zone, the Zhob convergence zone, and the Makran convergence zone (Lawrence et al., 1981). The Himalayan convergence is the northernmost zone and it has its southern boundary at the thrust faults of the Salt and Trans-Indus Salt Ranges. The southward over-thrusting has been estimated to be about 50 km (Sarwar and Dejong, 1979).

The Zhob convergence zone is mostly developed within the transform zone with strata characterized by intense folding (Lawrence et al., 1981). Southward thrusting along the Zhob fault has led to shortening in the area and the tectonic superposition of coeval formations of completely different facies suggests a minimal displacement of several kilometers (Lawrence et al., 1981).

East of Oman along the Makran convergence zone, the Arabian plate consists of oceanic crust that floors the Gulf of Oman and the adjacent Arabian Sea. The oceanic crust of the Arabian plate extends eastward to the Owen Fracture Zone along the Indian plate boundary, southward along the Gulf of Aden spreading center, and northward where it descends beneath the Eurasian plate at the trench lying offshore from the Makran (Lawrence et al., 1981). Farhoudi and Karig (1997) and Jacob and Quittmeyer (1979) have all interpreted this zone as a modern arc trench gap and consider the sedimentary fill to be a fore arc basin.

1.2 Previous Work

This study is part of a broader ongoing work aimed at a better understanding of the neotectonic characteristics of the relatively less studied Chaman fault in Pakistan using remote sensing techniques and geomorphometric measurements. Detailed works by Ul-Hadi (2012) in the northern segment (Figure 1.3) of the fault in Pakistan have shown numerous indications of recent fault activity in the area. Furuya and Satyabala (2008), in their work on a northern section of the fault in Afghanistan, have interpreted active fault movement in the area to be accommodating plate motion along the fault. Mohadjer et al., (2010) recorded slip rates of 5.2 to 18.1 mm/yr on the northern segments of the fault using GPS measurements. The Nushki segment represents the southernmost portion of the Chaman fault system and no known studies have been carried out on this segment of the fault. Thus, it is pertinent to study other parts of the fault (Nushki in the south) in order to determine similarities and contrasts in the tectonic behavior along different segments of the collision boundary.

1.3 Scope of work and objectives

The objectives of this work include;

i) To test the validity of geomorphic indices in neotectonic studies.

ii) To reconstruct the geomorphic evolution of landforms in the Nushki Basin using an integrated approach.

iii) To determine the direction of propagation of deformation due to active strike-slip faults and thrust faults in the Nushki Basin.

The Nushki Basin is a ~67 km long depression which lies along a segment of the Chaman fault that runs through western Pakistan and eastern Afghanistan. Lithology of sediments in the basin comprise of four different generations of alluvial deposits highly dissected by a set of linear stream networks (Figure 3.3). These deposits were generated from the erosion of the Khojak Pass Mountains. Three pop up zones exists in the basin; the northern ridge, the central ridge, and the southern ridge. Both the northern and central ridges are made of rocks belonging to the Spinatizha Crystalline Complex (SCC) of Lawrence et al., (1981) and Ul-Hadi, (2012). They also belong to rocks making up the Roghani Ridge as described by Ul-Hadi, (2012). The southern ridge is of a different lithology from the previously described ridges based on spectral characteristics observed from ASTER satellite images of the area. There exist various evidences of deformation of the alluvial deposits and displacement of blocks along the pop up zones all through the basin.

This study covers every part of the basin. However, specific details about rock lithology and locations of features were not covered as no field work was involved.

1.4 Methodology

Two main techniques were employed in this study; morphometric measurements using remote sensing and GIS tools. Remote sensing methods were employed to collect information about the general geology, structural trends, and geomorphology and drainage patterns in the area. Further processing, analysis and interpretation of the data was carried out using GIS tools to measure geomorphic indices, identify geomorphic changes, fault lines, and measure displaced blocks.

1.4.1 Remote Sensing and GIS Techniques

Remote sensing data of different resolutions were used in conjunction with GIS tools. ENVI 4.8 and ArcGIS 10 software were used for processing and analyzing satellite imagery respectively. The 3-D and spatial analyst tools in the ArcGIS suite enables processing of digital terrain models from DEMs using hillshade, aspect, stream networks, drainage basins, etc., while the ENVI is an advanced tool for geospatial image processing and analysis. It contains tools for automated processing of remote sensing data. The following remote sensing data were used in this study:

1.4.2 Digital Elevation Models (DEM)

Fifteen meter Digital Elevation Models (DEM) data of the area were created from ASTER stereo images. Satellite images draped over DEM data that provided a better view and understanding of the fault locations, geomorphic relationships and drainage patterns for a better understanding of neotectonic activity in the area. The DEMs also helped in giving near accurate measurements of elevation, distance, and indices of active tectonics.

1.4.3 ASTER Images

ASTER is an acronym for Advanced Spaceborne Thermal Emission and Reflection Radiometer. ASTER captures high spatial resolution data in 14 bands, from the visible to the thermal infrared wavelengths; and provides stereo viewing capability for digital elevation model creation. ASTER data are also valuable tools in the geomorphologic mapping of surface rocks, soils and bedrocks to study land surface processes.

1.4.4 Geomorphic Indices and Fluvial Signatures of Active Tectonics

The general geomorphic and fluvial systems in the Nushki Basin respond to transpressional motion in different ways manifesting as beheaded streams, stream offsets, channel deflection, offset alluvial fans, and linear drainage networks. Hence geomorphic and fluvial responses provide a valuable means of not only identifying areas of active tectonic activity but also measuring the displacement and uplift. These geomorphic and fluvial responses are normally expressed inform of changing drainage patterns, streams offsets, alluvial fan offsets, stream length gradient, changes in longitudinal profiles of rivers, river sinuosity, mountain front sinuosity, response of fluvial channels to lateral deformation, topography offset, and valley morphology (Keller and Pinter, 2002) . Geomorphic indices provide a quantitative method of studying, identifying, and classifying tectonically active areas. Three (3) geomorphic indices were calculated in this study; the stream length gradient index (SL), mountain-front sinuosity (Smf), and valley-floor width to height ratio (Vf). The SL index is a measure of stream power which controls its ability to erode its bed and transport sediment. It defined by $SL = (\Delta H/\Delta L)L$ where ΔH is the change in elevation of the reach, ΔL is the length of the reach and L is the total channel length from the midpoint of the reach of interest upstream to the highest point on the channel (Keller and Pinter, 2002). It is sensitive to channel slope, rock resistance, topography, and the length of the stream (Zovolli et al., 2004). Keller and Pinter, (2002) and Zovolli et al., (2004) have successfully used SL measurements in neotectonic studies in the San Gabriel Mountains of Southern California, U.S.A. and the Kompotades fault in Greece.

Mountain-front sinuosity is defined as Smf =Lmf/Ls; where Smf is the mountain-front sinuosity, Lmf is the length of the mountain front along the foot of the mountain at the pronounced break in slope and Ls is the straight line length of the mountain front (Keller and Pinter, 2002). It reflects the balance between erosional and tectonic activity affecting a mountain front. Low values of Smf are indicative of areas experiencing active uplift while high Smf values indicate areas more prone to erosional action.

The ratio of valley-floor width to valley height, Vf is defined as $Vf = 2Vf_w / [(Eld - Esc)] + (Erd - Esc)]$ where Eld and Erd are elevations of the left and right valley divides respectively and Esc is the elevation of the valley floor (Keller and Pinter, 2002). Broad-floored valleys have relatively high values of Vf associated with low uplift areas, while V-shaped valleys have low Vf values (close to 0) corresponding to rapidly incising valleys (Bull and McFadden, 1977; Zovoli et al., 2004).

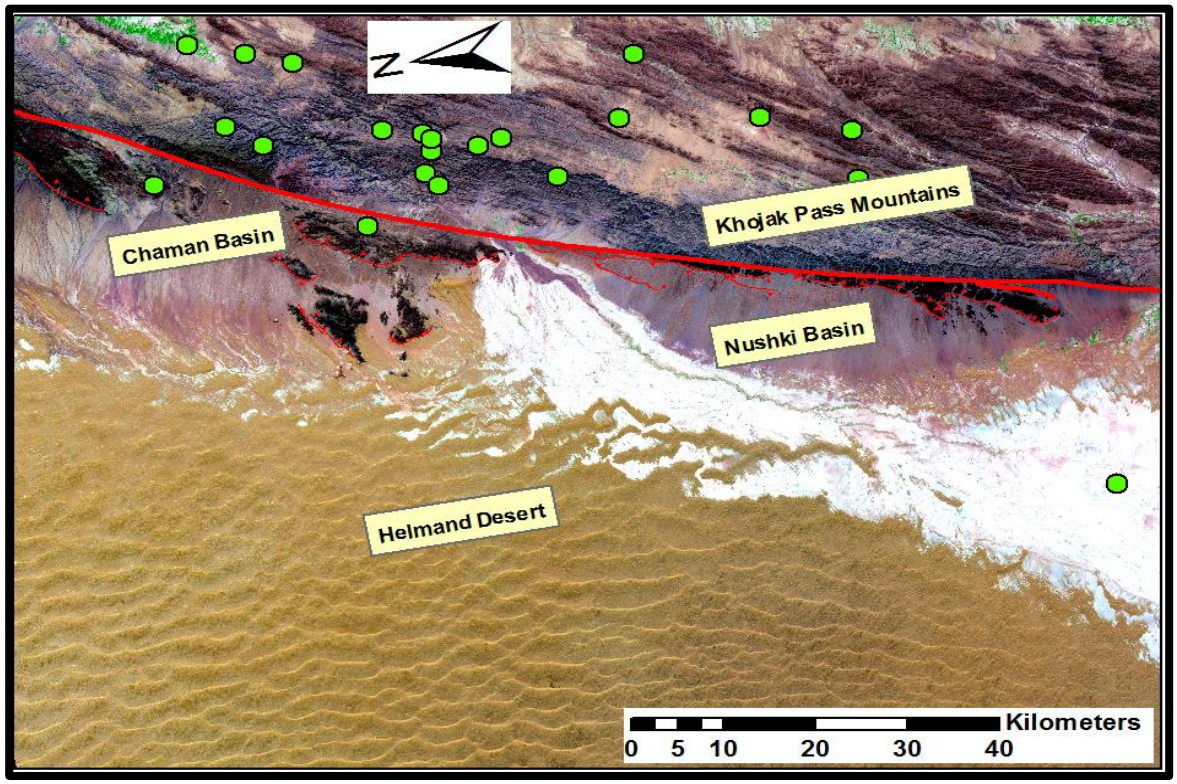

Figure 1.3: Landsat image showing the Chaman Basin (Ul-Hadi, 2012) and the Nushki Basin. The Khojak Pass Mountains which is the major source of sediments for the basins is located east of the main Chaman fault. Green circles are epicenters of historical earth quakes greater than magnitude 4. Note the near absence of such earthquakes in the Nushki Basin. There however exist evidences of recent tectonic activity in the area around the Nushki Basin.

CHAPTER 2: DATASETS AND METHODS

This study follows a quantitative morphotectonic approach. Primarily, 15m Digital Elevation Models (DEM) and satellite multispectral images were employed. Multispectral satellite data that were used included the Advanced Spaceborne Thermal Emission and Reflection Radiometer (ASTER) and, GeoEye-1 image data obtained from the Google Earth application. The aforementioned datasets greatly aided in geologic mapping of the study area, measurement of offsets, and calculations of geomorphic indices.

ENVI 4.8 and ArcGIS 10 software were employed in processing the datasets. The ASTER images were processed and used for geomorphic / geologic mapping of the area while the DEM was processed and used for measurement of geomorphic indices.

2.1 Geomorphic Indices and Tectonic Geomorphology

Geomorphic indices serve as very good indicators of the relative degree and rate of deformation in tectonically active zones. The effects of active tectonics in an area are usually expressed in the form of geomorphic changes on the surface. However, these changes might be on a very small scale hence making it invisible. Thus, results from calculations of geomorphic indices provide a better understanding of the rate and amount of deformation even on a very local scale. Generally, tectonic indices serve two main purposes; i) to quantify description of landscape, and ii) for rapid evaluation of tectonic activity in large areas. (Keller and Pinter, 2002). Geomorphic indices have been used to

acquire information about active tectonics in areas experiencing rapid deformation (Bull 1977, Keller and Pinter 2002, Zovoili et al., 2004).

Analysis of geomorphic indices used in this study was principally carried out using two very broad steps; i) visually identifying geomorphic landforms from satellite imagery, and ii) detailed measurements and statistical analysis of geomorphic indices using GIS tools to find areas showing anomalous values.

The effects of active tectonics in an area are usually expressed through geomorphic changes on the surface. Geomorphic indices and landform assemblages are useful in regional evaluations to identify relative tectonic activity and sites where rates of active tectonic processes may be evaluated (Keller and Pinter, 2002). This work aims to identify areas where these geomorphic changes manifest which will subsequently serve as pointers to the location of areas undergoing active deformation due to transpression. ASTER images were used to identify specific geomorphic features in the area. Geomorphic features identified include displaced and tilted alluvial fans, changes in stream pattern, stream offsets and general deformation in the continuity of the rocks units in the area (Figure 2.1).

Tectonic geomorphology is the study of landforms produced by tectonic processes, or the application of geomorphic principles to the solution of tectonic problems (Keller and Pinter, 1996). Tectonically active zones are usually characterized by a host of geomorphic expressions on the surface depending on the predominant type of surface deformation the area is undergoing. These features range from beheaded streams, stream offsets, deposition style of alluvial fans, drainage style, water gaps, and wind gaps.

Processed ASTER scenes (Figure 2.2) from the area clearly show these geomorphic features which support recent tectonic activity in the Nushki Basin.

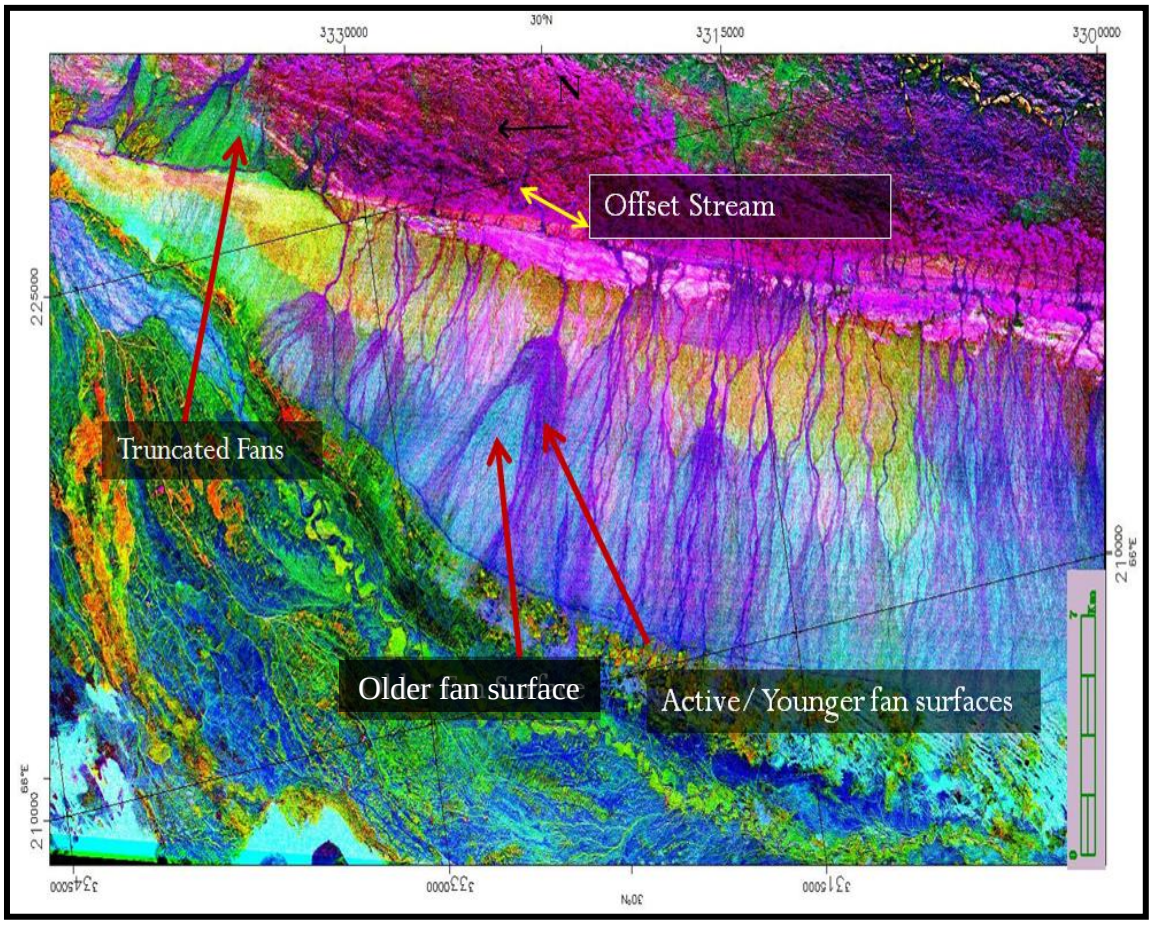

Figure 2.1: ASTER false color (RGB band combination 3-1-2) image of parts of the Nushki Basin showing the different geomorphic features in the basin.

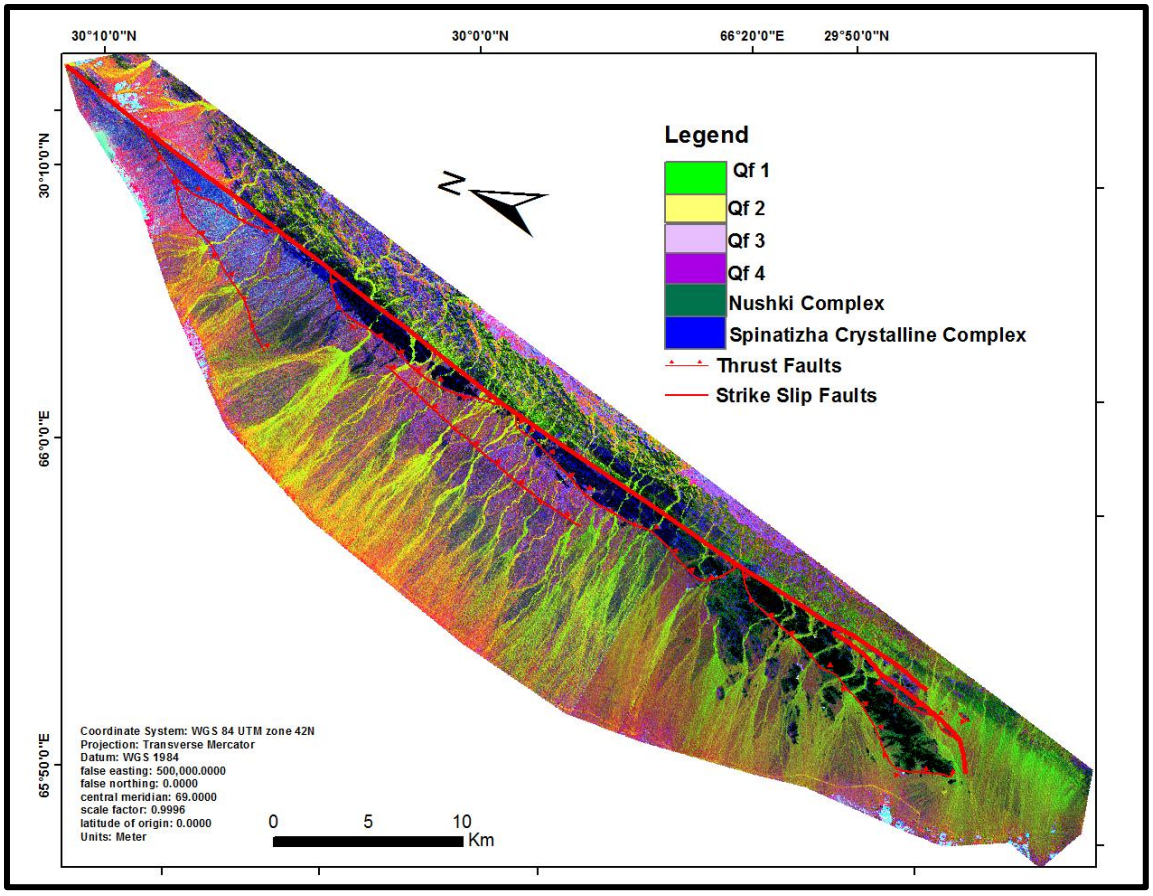

Figure 2.2: ASTER derived false color composite image (RGB band ratio 5/7, 5/1, 5/4, with USGS 1 enhancement) of the Nushki Basin showing the general lithologic units along with major strike slip and thrust faults. Three generations of alluvial fan deposits have been identified along with two distinct crystalline complexes.

Fifteen meters ASTER DEMs were created to aid in calculating geomorphic indices and specifically displacements of blocks and vertical uplifts. The drainage pattern serves as a pointer to the type of deformation an area is undergoing. The dominant drainage patterns identified from the ASTER images are straight parallel streams in an E-W direction.

Useful geomorphic indices used in evaluating tectonic activity are stream length gradient index (SL), the ratio of valley floor width to valley height (Vf index), both developed by Bull and McFadden (1977), and mountain front sinuosity. The SL index and Valley floor

width to height ratio (Vf) have been widely used by various workers in different parts of the world to study relative tectonic activity. However, most of these studies are done using only topographic maps and aerial photographs. This project utilizes satellite images (ASTER), Digital Elevation Models and GIS tools in studying these changes and calculating geomorphic indices.

Three (3) geomorphic indices were calculated; valley floor width to height ratio (Vf), stream length gradient index (SL), and mountain-front sinuosity (Smf).

2.1.1 Stream-length Gradient Index (SL)

The SL index provides a measure of the erosional resistance of the rocks involved and relative intensity of active tectonics (Hack, 1973; Keller and Pinter, 2002) and is defined as:

$SL = (\Delta H/\Delta L)*L$

Where $\Delta H/\Delta L$ is the channel gradient of a particular reach of a stream (ΔH is the change in elevation along the length (ΔL) of the reach) and L is the total length of the channel from the midpoint of the reach to where the index is calculated upstream to the divide.

2.1.2 Mountain-front Sinuosity (Smf)

Mountain-front sinuosity is defined as: $Smf = Lmf / Ls$

where Smf is the mountain-front sinuosity, Lmf is the length of the mountain front along the foot of the mountain at the pronounced break in slope, and Ls is the straight line length of the mountain front (Keller and Pinter 2002). It reflects the balance between erosional and tectonic activity affecting a mountain front. Low values of Smf are

indicative of an area experiencing active deformation while high Smf values indicate erosional action. It characterizes the morphology of the mountain front along border faults (Peters and van Balen, 2007). Smf values close to 1.0 are related to the most tectonically active fronts while a reduction or cessation in the rate of uplift leads to increased Smf values. Thus, erosional processes begin to form a sinuous front which becomes more irregular with time. (Ramirez-Herrera, 1998)

2.1.3 Valley-floor Width to Height Ratio (Vf)

The valley-floor width to height ratio (Vf) is defined as

$$Vf = 2Vfw / [(Eld - Esc)] + (Erd - Esc)]$$

where Eld and Erd are elevations of the left and right valley divides respectively and Esc is the elevation of the valley floor (Keller and Pinter, 2002). Broad-floored valleys have relatively high values of Vf that is associated with low uplift areas, while V-shaped valleys have low Vf values corresponding to rapidly incising valleys (Bull and McFadden, 1977; Azor et al., 2002). Vf reflects the differences between the V-shaped valleys which are downcutting in response to active uplift, where the stream is governed by the influence of a base-level fall at some point downstream that indicates a relatively high tectonic activity, and U shaped broad-floored valleys with principally lateral erosion into the adjacent hillslopes in response to relative base-level stability or tectonic quiescence that signifies a relatively low tectonic activity. Thus, Vf uses one vertical and one horizontal dimension at a given point along the stream in the erosional system (Keller and Pinter, 2002; Ata, 1998; Tsodoulus et al., 2008).

2.2 Landforms Associated with Active Deformation

Strike-slip and thrust fault interaction is common in the area and there exist characteristic landforms associated with this kind of fault interactions (Figure 2.2). The pattern of stream channel orientation, pattern of alluvial fan deposition and other geomorphic landforms in the area were studied and they served as good pointers to areas undergoing active deformation.

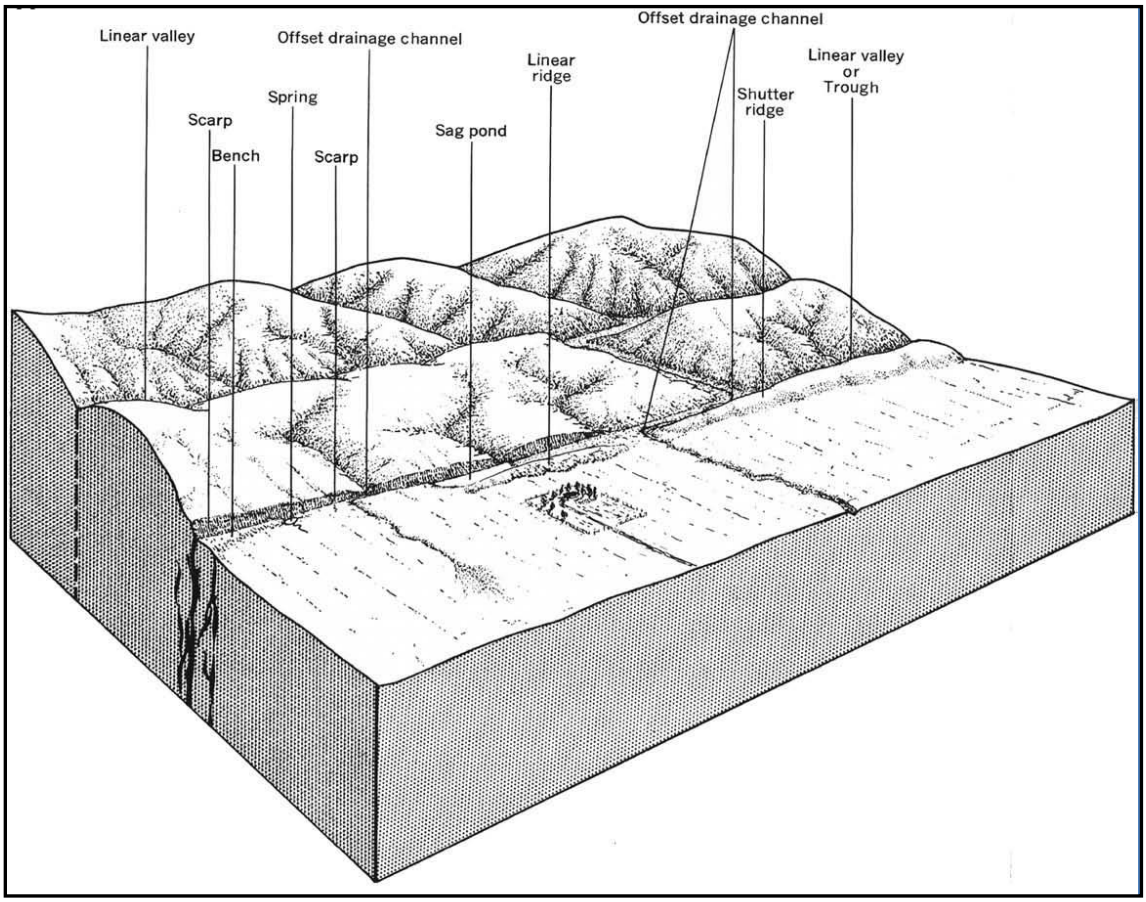

Figure 2.3: Major landforms associated with active strike-slip faulting (After Wesson et al., 1975)

2.2.1 Stream Offsets and Linear Valleys

Stream offsets are landforms which characterize areas where strike-slip faulting is prevalent. Strike-slip motion along a fault causes streams flowing oblique to the main fault line to become deflected to flow parallel to the main fault line and then returns to its original pattern after some distance (Figure 2.1). The stream pattern in areas undergoing active deformation usually manifest in form of linear valleys, as can be observed from Figure 2.1. This pattern of stream flow usually manifests its self as a series of linear valleys perpendicular to the main fault line (Keller and Pinter, 2002).

2.2.2 Drainage Pattern

Streams draining the area of study show a general transition from bedrock channels into alluvial channels, each with their characteristic drainage pattern. However, bedrock channels are relatively less sensitive indicators of local tectonic deformation due to the general lack of grading of streams as can be seen in alluvial channels. Thus, alluvial channels could be described as straight, meandering, or braided and tectonic processes could cause a change in the character of these channels (Keller and Pinter, 2002).

Tectonic activity and lithology of rocks play a huge role in the type of drainage pattern found in any particular location. Thus drainage patterns can be said to be more or less a visible manifestation of the degree or type of tectonic activity. Generally, dendritic drainage patterns form in areas where the streams flow over horizontal beds in areas with gentle regional slope; parallel drainage pattern are commonly found in areas of moderate to high slopes where bedrock and other landforms tend parallel to the regional slope (Keller and Pinter, 2002). Trellis drainage patterns form in areas where there are dipping

or folded sedimentary, volcanic, or low-grade metasedimentary rocks, and areas of parallel fractures (Howard, 1967). Radial drainage patterns form in area of structural high such as volcanoes, salt domes or tectonic upwarps (Table 2.1, Figure 2.4). Drainage maps generated from ASTER 15m DEM shows a predominantly parallel drainage pattern in the area.

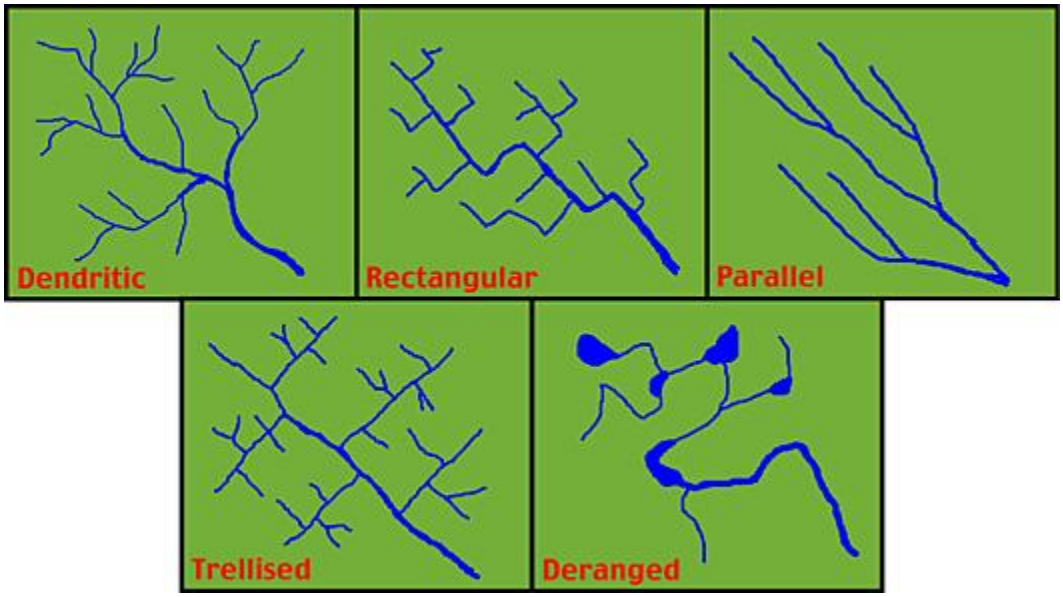

Figure 2.4: Common drainage pattern types (Source: Pidwirny, 2006)

Table 2.1 Classification of Drainage Patterns (Modified from Howard, 1967)

Pattern	Significance
Dendritic	Horizontal sediments or uniformly resistant crystalline rocks; gentle regional slope at present or at time of drainage inception
Parallel	Moderate to steep slopes; also in areas of parallel elongate landforms
Trellis	Dipping or folded sedimentary, volcanic, or low-grade metasedimentary rocks; areas of parallel fractures
Rectangular	Joints and/or faults at right angles; streams and divides lack regional continuity
Radial	Volcanoes, domes, and residual erosion features
Annular	Structural domes and basins, diatremes, and possibly stocks

2.2.3 Water Gaps and Wind Gaps

Water gaps and wind gaps are very important geomorphic features which help in getting a better understanding of the direction of lateral propagation of faults or folds. Water gaps are formed as a result of river incisions thereby increasing the surrounding relief and topography. On the other hand, wind gaps are formed when the rate of continuous uplift of a structure through which a river flows far exceeds the rate of down cutting by the river thus forcing it to flow towards a new path around the structure. Hence, the abandoned notch on the ridge which initially began as a water gap now becomes a wind gap. (Keller and Pinter, 2006).

2.3 Advanced Spaceborne Thermal Emission and Reflection Radiometer (ASTER)

ASTER was developed by the National Aeronautics and Space Administration (NASA) and the Japanese Ministry of Economy Trade and Industry (METI). The instrument is onboard the Earth Observing System (EOS) TERRA satellite which was launched in December 1999. It records data in three (3) different segments of the electromagnetic spectrum; Visible and Near Infra-Red (VNIR), Shortwave Infra-red (SWIR), and Thermal Infra-red (TIR). There are a total of fifteen (15) spectral bands amongst them with distinct wavelength ranges of 0.53-0.86μm, 1.60-2.43μm, and 8.13-11.65μm, respectively. The VNIR segment has four (4) bands with 15m resolution which also includes a backward looking telescope (Band 3b) which is very useful DEM extraction and stereo pair generation. There are six (6) SWIR band each with 30 m resolution. The

TIR has five (5) bands with 90m resolution (Yamaguchi et al. 1998). Data collected in all ASTER bands are collected in swaths of 60m x 60m.

2.4 GeoEye-1

The GeoEye-1 was launched in 2008. It is a commercial satellite used to acquire multi directional images of the earth's surface in panchromatic and multispectral modes with ground resolutions of 0.41 m and 1.65 m respectively. GeoEye images are available in panchromatic, multispectral, and pan-sharpened imagery. Panchromatic images are collected in the broad visual wavelength range, and then rendered in black and white to show contrast and detail. Multispectral images are simply full-color photographs, while pan-sharpened images are multispectral photographs that have been sharpened by the panchromatic information collected (www.geoeye.com).

The panchromatic mode has a spectral resolution of 450-800 nm while that of the multispectral mode is 450-920 nm, both in the visible and near infrared (VNIR). GeoEye-1's panchromatic image resolution of 0.41 m (about 16 inches) means we can see very small objects. Once a panchromatic image is collected by GeoEye-1, it is resampled to 0.50 m resolution according to the operating license. These are the clear, accurate images that online (e.g. Google Earth) maps users most often associate with GeoEye (www.geoeye.com). GeoEye imagery, due to its very high resolution, is very useful in detailed studies of landforms. Imagery used for this work was obtained from the Google Earth platform.

2.5 Digital Elevation Models (DEMs)

Digital Elevation Model (DEM) is a raster grid of elevation values that represent a surface. They are useful for many applications, including mapping and orthorectification (www.envi.com). They are used also for creating contour maps, hillshades, aspect, and slope maps.

Computer-based geomorphometry using DEMs allow for the analysis of three-dimensional properties of landscape (Font, 2010) especially in areas where field work is difficult to carry out due to accessibility such as western Pakistan.

A variety of techniques can be used for DEM creation. These include extraction by digitizing topographic maps, spaced gridded data derived from digital photogrammetry, and from digital image stereo pairs (Tsodoulos et al., 2008). DEMs for this work were generated from panchromatic ASTER stereo images 3N and 3B, both with 15m resolution (Figure 2.4). The generated DEM served as the basic dataset for shaded relief image generation, slope analysis, aspect analysis, stream network and stream density analysis, and topographic analysis.

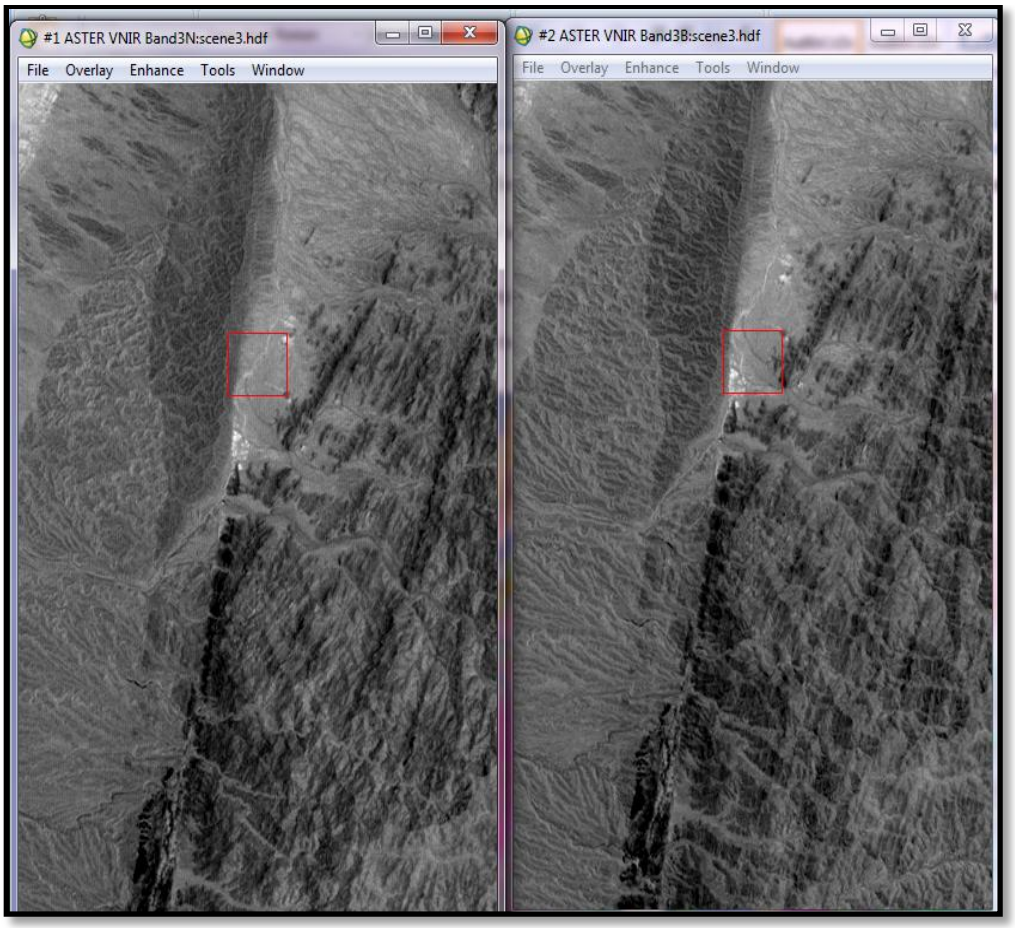

Figure 2.5: ASTER grey scale stereo image pairs 3N and 3B used for DEM creation

2.6. Remote Sensing Techniques

2.6.1 Geologic/Geomorphic Mapping

The relationship between various lithologies is very useful in geomorphic analysis as most indices are controlled or affected by lithologies of the predominant rock units in the area. Different processing techniques were employed in order to get a more lucid picture of the relationships between different rock lithologies, faults and the drainage networks in the area. Two ASTER scenes covering the study area were used. Brief descriptions of the various processes employed are given below.2.6.2 Mosaics

This is the simple combination of different image scenes to become a single image (Figure 2.5).

Figure 2.6: ASTER scene images (RGB band combination 3-2-1) of the study area before mosaicking to form a single image .

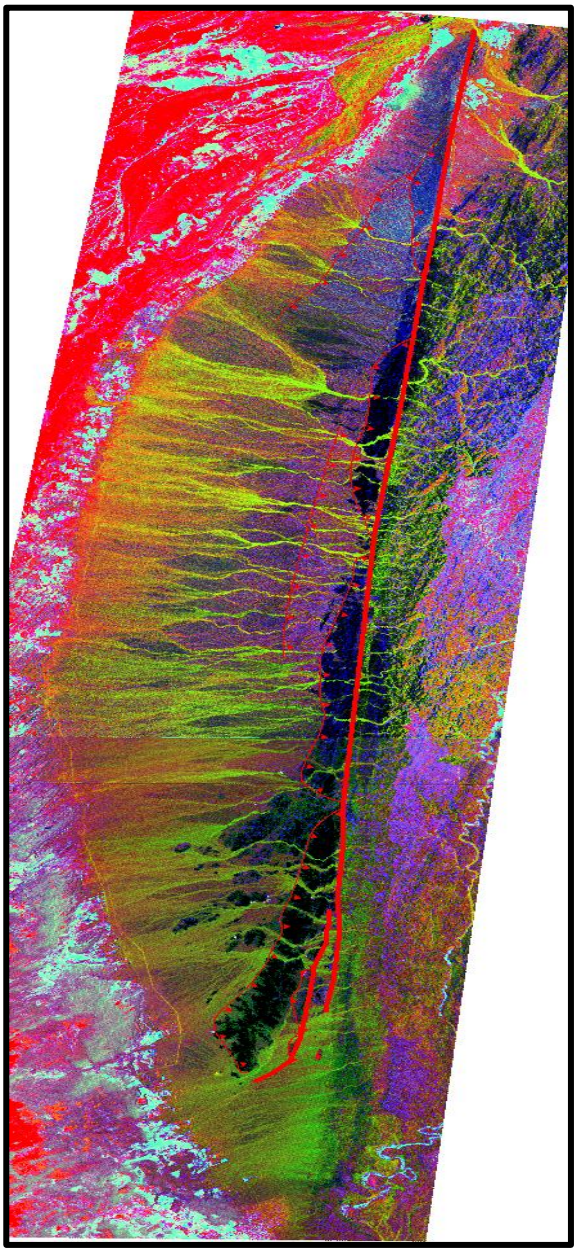

Figure 2.7: ASTER images (RGB band ratio 5/7-5/1-5/4 with USGS 1 enhancement) in Figure 2.6 after mosaicking.

2.6.3 Band Math/Band Ratio

This involves either dividing one band by another band using an algorithm in the ENVI software or multiplying one band by another band. The main aim of applying band ratios

to images is to enhance differences between bands which represent spectral features of interest while suppressing other features. For this study, we are interested in the response of morphology of fan surfaces, drainage systems and, the general landform to active deformation of the area. Thus, ASTER bands 1, 4, 5, and 7 which are very useful in delineating rock lithology and water bodies were used in calculating the band ratios to produce a better enhanced image of the area. Band ratios of 5/7, 5/1, and 5/4 were applied as the RGB combination respectively.

2.6.4 Interactive Stretching

This is an enhancement technique which aids/improves interpretation of the various geologic features and rock lithologies in the image. It involves altering the contrast among various bands to improve visualization. The equalization technique produced the best results. Stream patterns and different generations of alluvial fans were easily distinguished.

The image was filtered using the following parameters: Filter type: 5x5; Convolution: 40% add-back, kernel size 5 in order to remove speckles so as to give a very clear image (Figure 2.7).

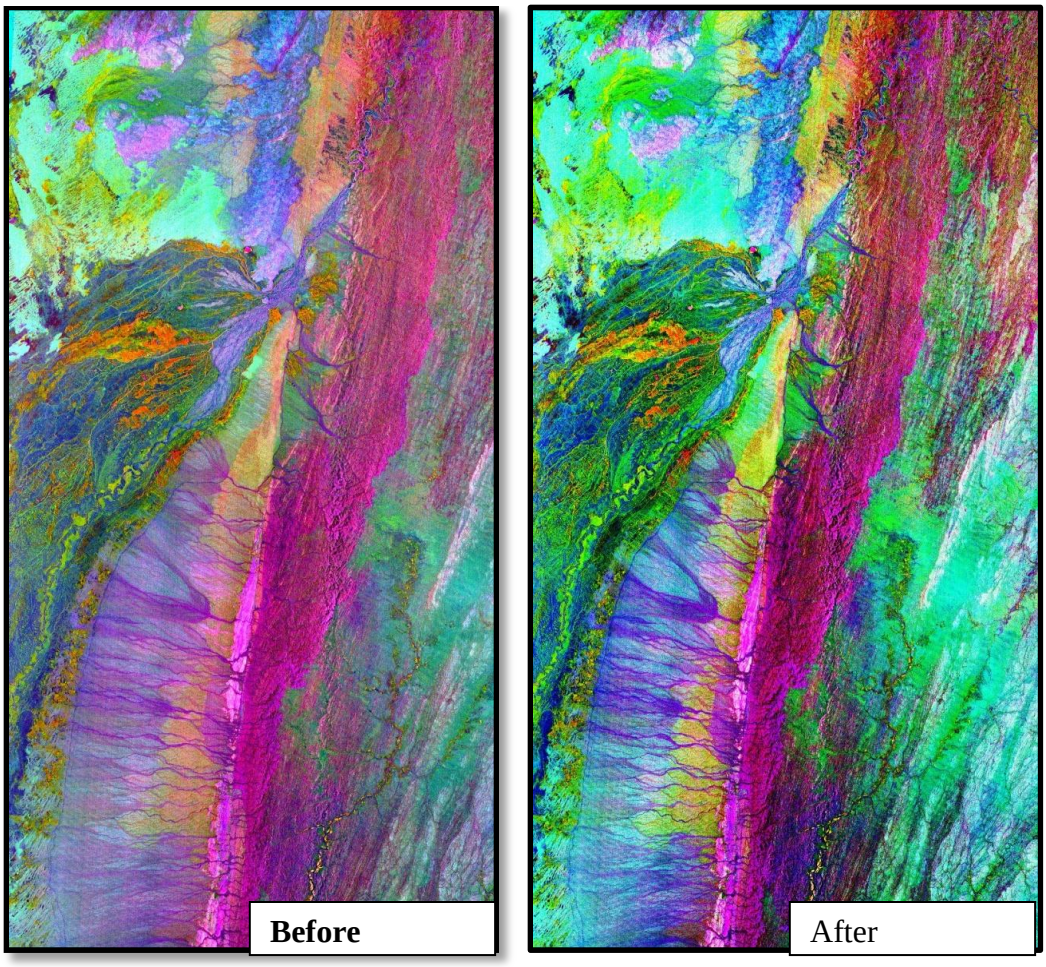

Figure 2.8: Before and after interactive stretching images of the study area. Note how the image becomes visually clear in the after image, thus highlighting the different lithologies better. (RGB band ratio 5/7-5/1-5/4 with no enhancement)

2.6.5 DEM Creation from ASTER Stereo Images

Digital Elevation Models are very important data in morphometric calculations and the resolution plays a very important part measurements of tectonic indices. The DEM extraction tool in the ENVI software is very useful for this purpose. It has the functionality that enables elevation data to be extracted from ASTER stereo imagery to create DEMs. The process requires stereo pairs of images containing rational polynomial coefficients (RPC) positioning from the sensors . The RPC are then used to generate tie points and calculate the stereo image pair relationship.

Two ASTER stereo image pairs (bands 3N and 3B) in grey scale from the area were used for DEM creation (Figure 2.4).

ASTER uses the visible near infrared (VNIR) telescope's normal (3N) and backward (3B) viewing bands for along-track stereoscopic observation. The second step involves defining tie points. This is done so as to define the relationship between the stereo images. Thus, tie points are generated and used to define epipolar geometry and create epipolar images. Tie points could be defined in one of 3 ways: automatically, by interactively defining tie points manually, and by reading tie points from a file already generated (Figure 2.9) .

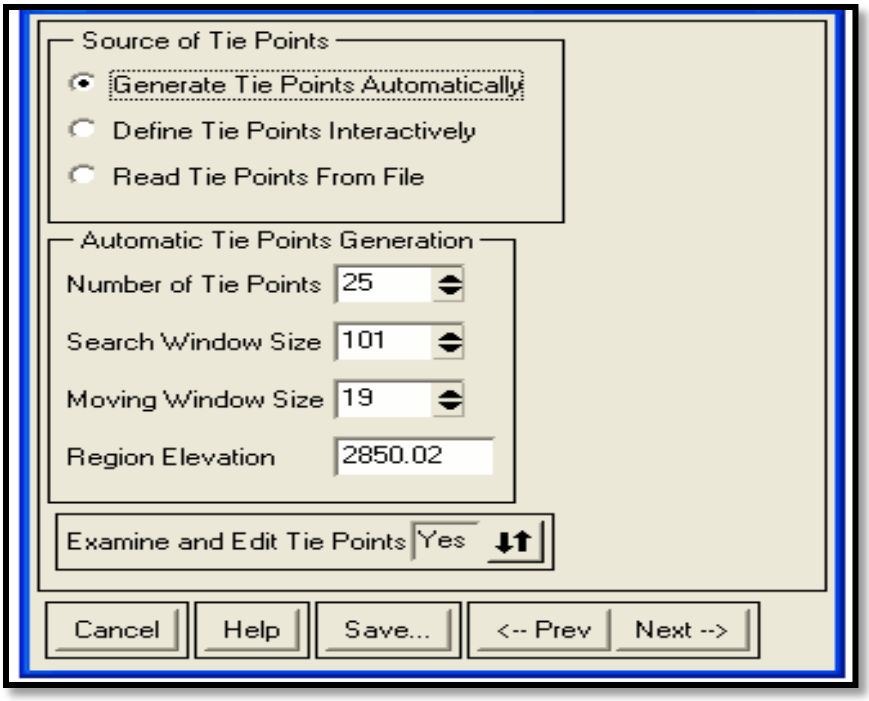

Figure 2.9: Generating tie points for DEM creation using the ENVI software.

For this work, tie points were generated automatically (Figure 2.8) as it gives a more accurate result with very little root mean square (RMS) error of less than 2. Another advantage of the manual method is, the tie points could be edited so as to reduce the margin of error. Epipolar geometry and images which will be used to extract the DEM were then calculated using ENVI. Epipolar images shows the relationship between the pixels in the stereo pair The final step involves specifying the DEM parameters (output projection and extraction parameters). These parameters could be the pixel size, projection type, image size, minimum correlation, edge trimming, and terrain relief (Figure 2.9).

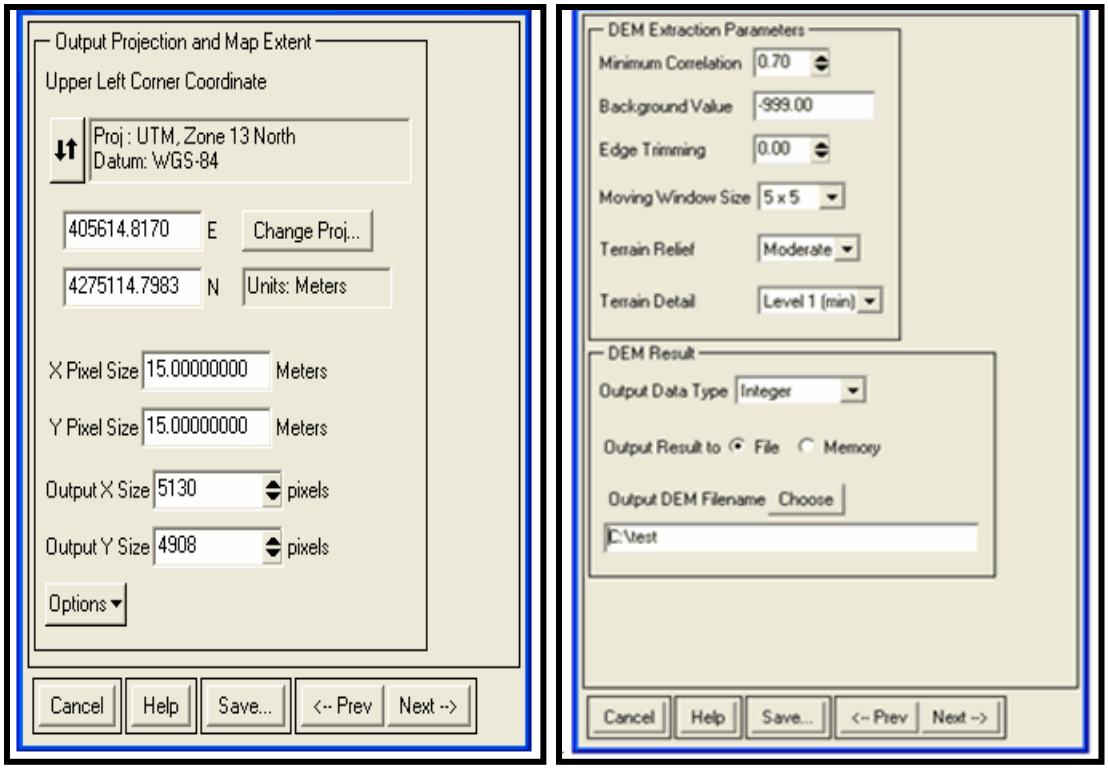

Figure 2.10: Output parameters for DEM extraction in ENVI 4.0. The WGS 1984 datum on the utm projection was used for generating the DEMs in this work.

2.7 GIS Techniques

ArcGIS is a useful software application for displaying, maesuring, and analyzing geospatial data. The 15m DEM earlier extracted from ASTER stereo images and the processed ASTER images were the major input data used here. The ARCGIS sofware suite was mainly used in geologic mapping of faults, lithology, slopes, and aspect ratio in the area and for calculating geomorphic indices. Various processes carried out on the extracted DEM using the ArcToolbox option on ArcGIS. These are briefly explained below.

2.7.1 Stream Network Extraction

Stream network extraction enables for the analysis of drainage patterns and calculations of the stream-length gradient index (SL) and the valley floor width to height ratio (Vf). It involves several steps using the hydrology tool on the ArcGIS suite. The first step in DEM processing using ArcGIS is filling parts of the the DEM which might erroneously show zero values called 'sinks'. Sinks are cells with unidentified drainage directions. Hence, the **'fill'** sub-tool under the hydrology tool was used to correct this anomaly. The aim of filling sink cells to the pour point (the boundary cell with the lowest elevation for the contributing area of the sink).

The next step is the generation of a flow direction raster. The 'flow direction' sub-tool creates a raster of flow direction from each cell to its steepest downslope neighbor. The output of the flow direction tool is an integer raster whose values range from 1 to 255. If a cell is lower than its eight neighbors that cell is given the value of its lowest neighbor, and flow is defined toward this cell. If multiple neighbors have the lowest value, the cell is still given this value. This is used to filter out one-cell sinks, which are considered noise (ArcGIS 10.1 help).

The '**flow accumulation'** sub-tool creates a raster of accumulated flow into each cell. The result of flow accumulation is a raster of accumulated flow to each cell as determined by accumulating the weight for all cells that flow into each downslope cell. Cells of undefined flow direction will only receive flow; they will not contribute to any downstream flow. A cell is considered to have an undefined flow direction if its value in

the flow direction raster is anything other than 1, 2, 4, 8, 16, 32, 64, or 128. The accumulated flow is based on the number of cells flowing into each cell in the output raster. Output cells with a high flow accumulation are areas of concentrated flow and can be used to identify stream channels. Output cells with a flow accumulation of zero are local topographic highs and can be used to identify ridges.

The **'stream order'** sub-tool is used to assign a numeric order to links in a stream network. This order is a method for identifying and classifying types of streams based on their numbers of tributaries. Some characteristics of streams can be inferred by simply knowing their order (Tarboton, et al., 1991). Hence, it is easy to pick major streams for calculating the stream-length gradient index.

The **'stream link'** sub-tool assigns unique values to sections of a raster linear network between intersections. Links are the sections of a stream channel connecting two successive junctions, a junction and the outlet, or a junction and the drainage divide (ArcGIS 10.1 help).

Finally, a threshold of stream network was created using the **'map algebra'** sub-tool to highlight the major streams and their tributaries. A threshold of 3000 produced the best results. The threshold used ensures that a stream starts at a pixel which 3000 upslope pixels flow into (Figure 2.10). Fifty meter (50m) elevation contours were also created from the DEMs using the contour tool. The contours will greatly aid in calculating SL index values for different stream segments.

To fully understand the behavior of streams in the area in response to active faulting, drainage basins were extracted from the DEM. A total of six (6) drainage basins were identified (Figure 2.11).

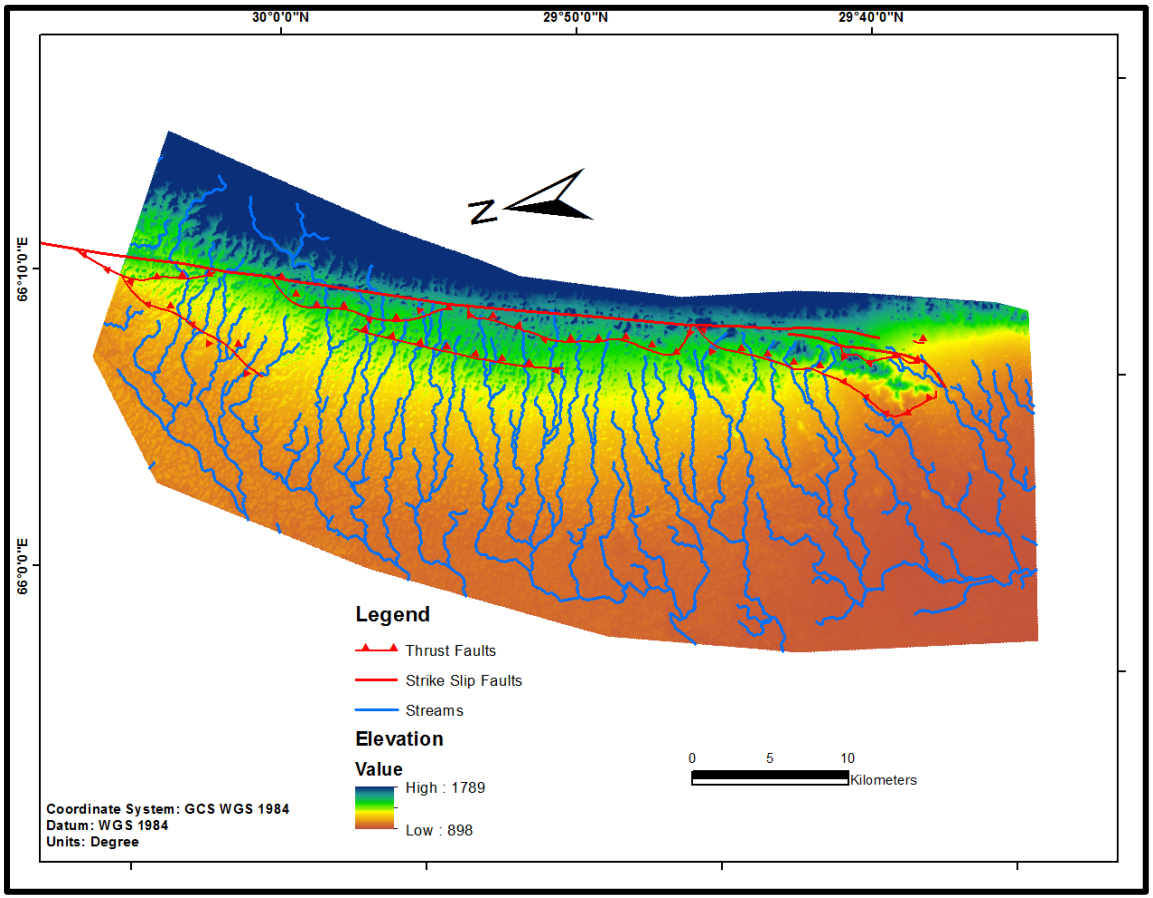

Figure 2.11: Vectorized stream network map draped over a DEM. The drainage pattern in the basin is generally the parallel pattern.

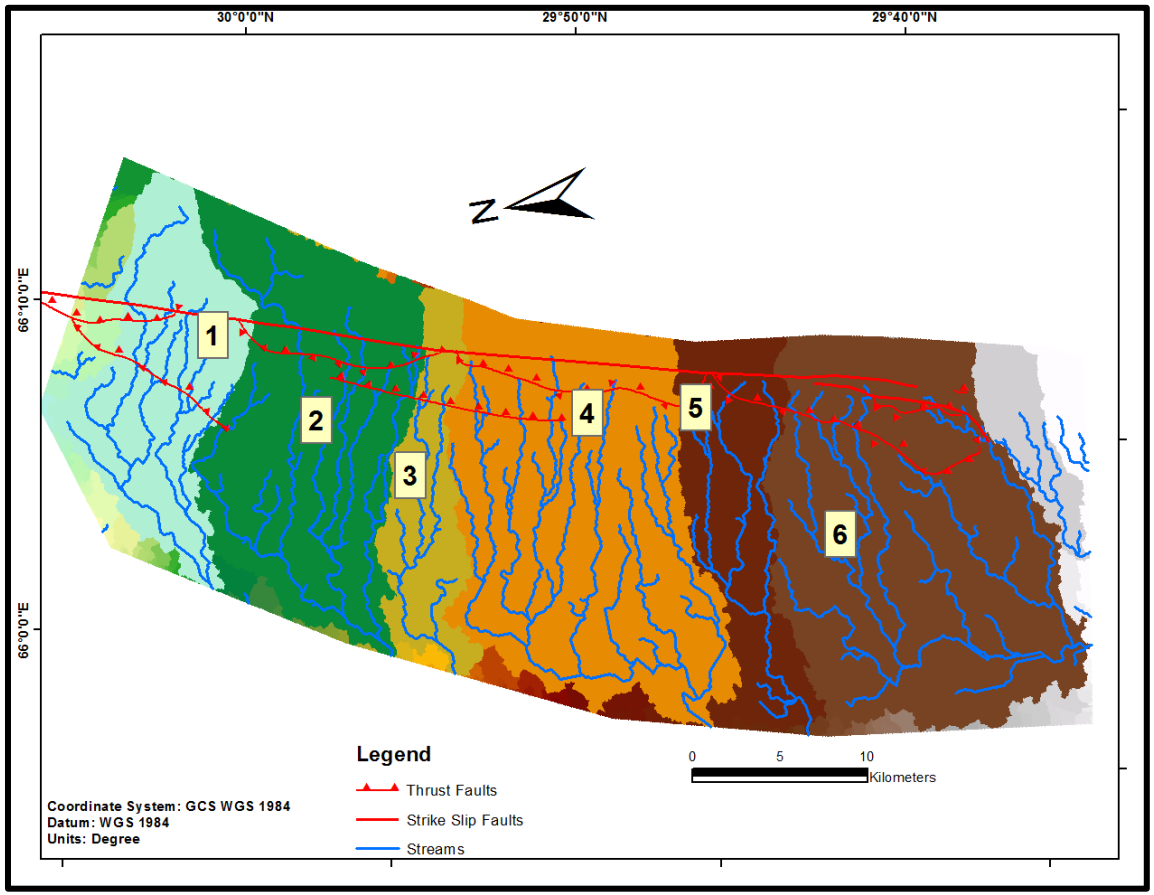

Figure 2.12: Drainage basins generated from DEM**.** A total of six drainage basins were identified.

CHAPTER 3: RESULTS

3.1 Geomorphic Mapping

Different band combinations and enhancement tools discussed in chapter two were applied in order to distinguish the different lithologies and to better to enhance better visualization of the geomorphic landforms present in the area. Four different generations of alluvial fans were mapped based on the distinct spectral characteristics observed from the ASTER images (Figure 2.2). Visually, the contrast in spectral properties appears as different colors. The relatively less deformed fans (Qf 1 and Qf2) are the youngest generation while the highly dissected and uplifted fans are of the older generation.

Three ridges bounding the basin were identified namely the northern ridge, central ridge and southern ridge. They all lie east of the main Chaman fault (Figure 3.1). The northern ridge and the central ridge show similar spectral characteristics while the southern ridge displays a different spectral characteristic. Numerous beheaded streams and steam deflections were observed in the Nushki Basin. These are very good indicators of active strike-slip faulting.

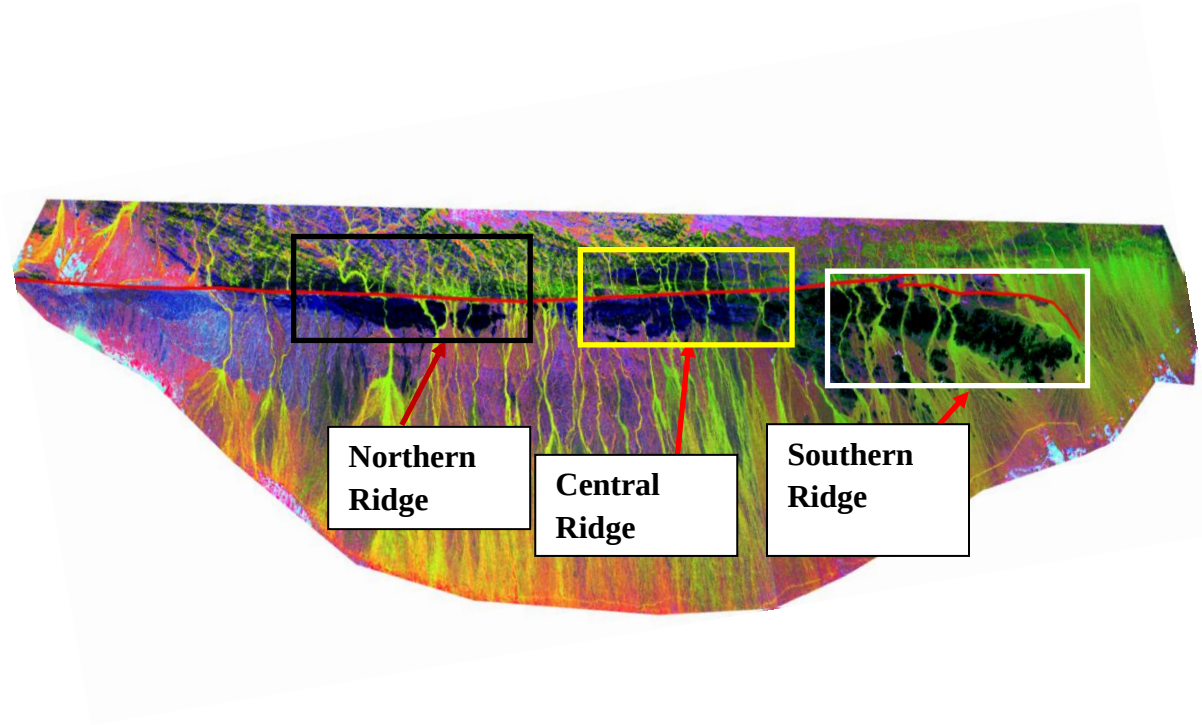

Figure 3.1: Locations of three ridges along the main Chaman fault making up the mountain fronts in the Nushki Basin. The black box represents the northern ridge; yellow box represents the central ridge, while the while box represents the southern ridge.

3. 2 Offsets and Displacements

3. 2.1 Stream Offsets:

Stream offsets are landforms which characterize areas where active strike-slip faulting is prevalent. Strike-slip motion along a fault causes streams flowing oblique to the main fault line to become deflected flowing parallel to the main fault line and then returning to its original pattern after some distance. One major stream offset was identified on the main antecedent stream flowing along the northern mountain front (Figure3.2). There also appears to be an earlier displacement of the antecedent stream due to differential uplift of the northern ridge. Measured offset plus the displacement is 2384 m, with the offset accounting for around 1000 m of the measured displacement along the northern mountain front.

3.2.2 Alluvial Fan Offsets:

The Nushki Basin is filled with sediments sourced from areas east of the Khojak Pass Mountains. Sediments in the basin based on ASTER image interpretation are mostly siliclastics with intrusions of crystalline complexes as a result of uplift. Four generations of alluvial fans have been identified (Figure 2.2). The youngest generation Qf1, appears lemon green in color on the ASTER false color composite image and is found in abundance on the southern flanks of the basin, the second youngest set of fans Qf2, appears yellowish green on the ASTER false color composite image and are deposited further north of Qf1. They underlay the older generation of fans Qf3 and Qf4 (light purple and pink respectively). Fans on the northern flank and central portions of the Chaman Basin are relatively stable while the youngest generations of fans Qf1, on the

southern flanks appears to have been heavily deformed showing large scale tilting, numerous offsets, and dissection by streams. However, it was only possible to match only one offset fan surface as many fan surfaces in the area have either been affected by erosion or highly deformed. Total offset recorded on the offset fan is about 235 meters. (Figure 3.5).

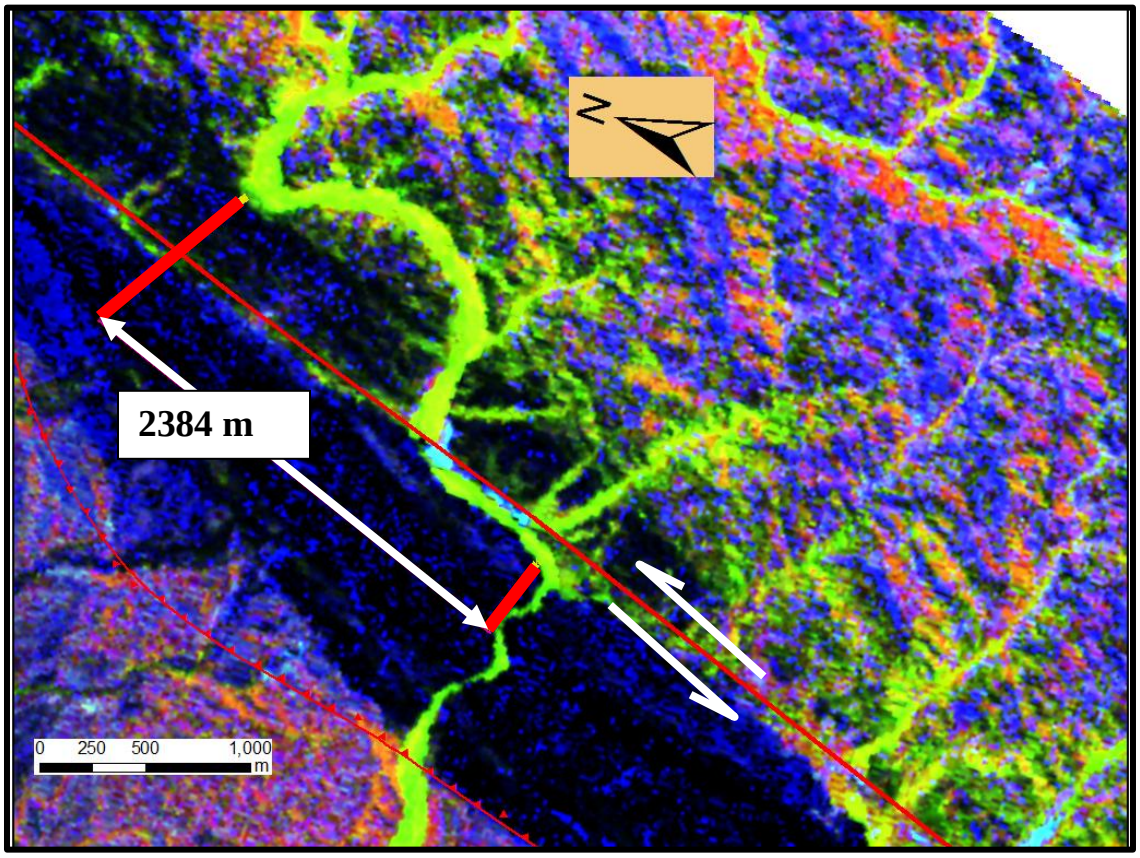

Figure 3.2: Stream offset along a ridge on the northern mountain front of the Nushki Basin. Measured offset (white line) is approximately 2384 meters along the ridge. (RGB band ratio 5/7, 5/1, 5/4 with USGS 1 enhancement)

3.2.3 Offset Blocks

The ridge north of the basin which is part of the Roghani ridge of Lawrence (1981) and Ul-Hadi (2012) lies along the major strike-slip fault in the area. Spectral analysis from ASTER imagery shows the same rock units of the Roghani ridge across both sides of the strike-slip fault. Careful analysis and observation of the ridge shows a left-lateral offset of about 6980 m (Figure 3.3 and Figure 3.4).

A unit of clastics interspersed with crystalline rocks of the Nushki complex located along the southern flanks of the basin was discovered to have shown some form of offset. The offset movement was also along the strand of the Chaman strike-slip fault in the southern part of the Nushki Basin. A lateral offset of about 2015 m was measured (Figure 3.6 and Figure 3.7).

A summary of the major offsets recorded is given in Table 3.1.

Table 3.1: Recorded offsets in the Nushki Basin.

S/no	Offset Feature	Displacement (m)
1	Part of the Roghani Ridge	6980
2	Deflection of stream along Roghani Ridge	2384
3	Ridge located south of the Nushki Basin	2015
4	Alluvial fan south of the Nushki Basin	235

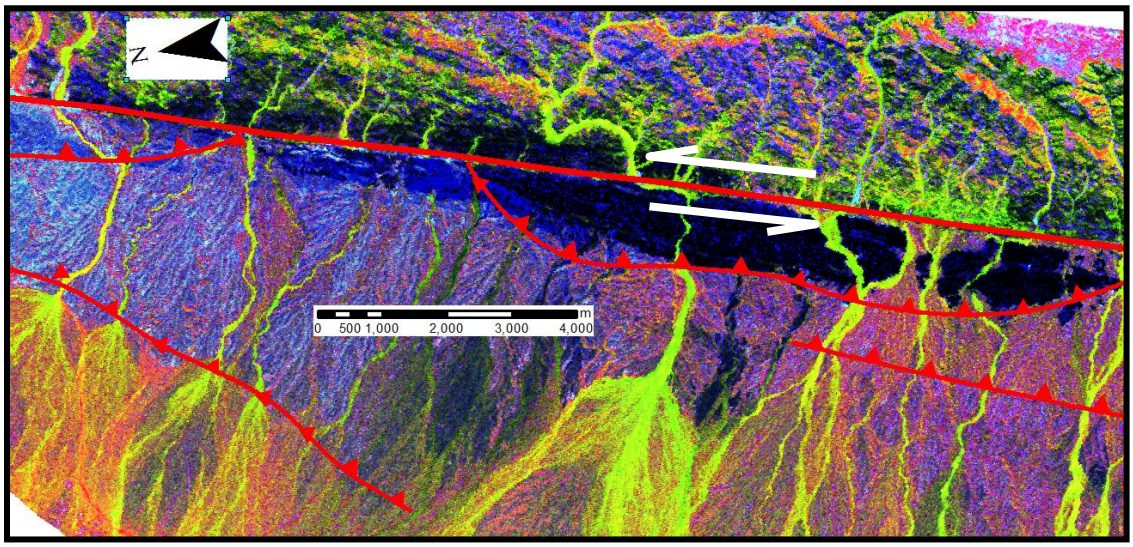

Figure 3.3: ASTER false color composite image of the northern ridge showing left lateral block (dark blue) offset along the Chaman fault. This offset might be responsible for the deflected stream.

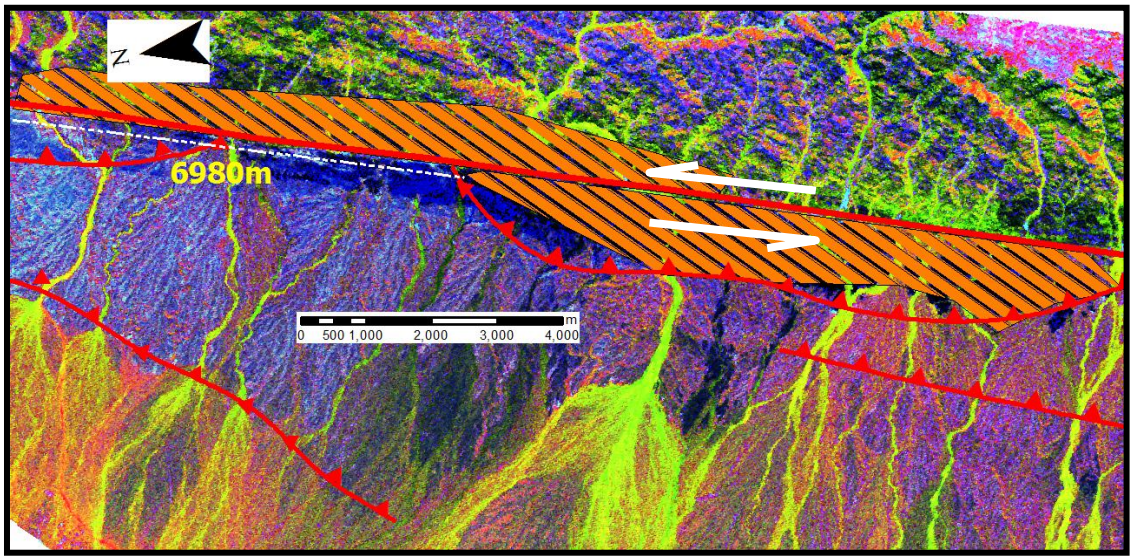

Figure 3.4: Measured displacement along the northern ridge on ASTER false color image (RGB band ratio 5/7, 5/1, 5/4 with USGS 1 enhancement). A left lateral displacement of 6980 meters was recorded.

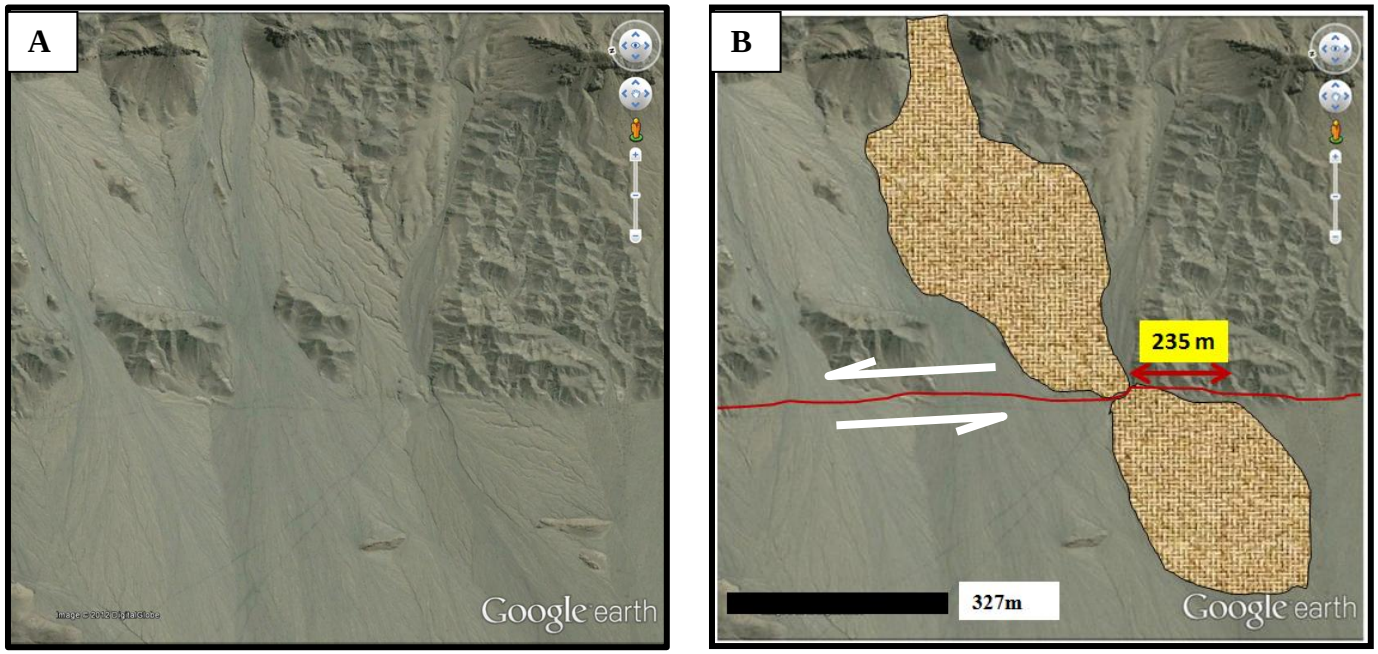

Figure 3.5 (A & B): Alluvial fan offset on the southern flanks of the Nushki Basin. The area shows numerous deformations of alluvial fans along with stream dissection. Matching of offset fan surfaces was difficult due to the intense amount of deformation in the area. The offset surface shown above (B) recorded a displacement of 235 meters.

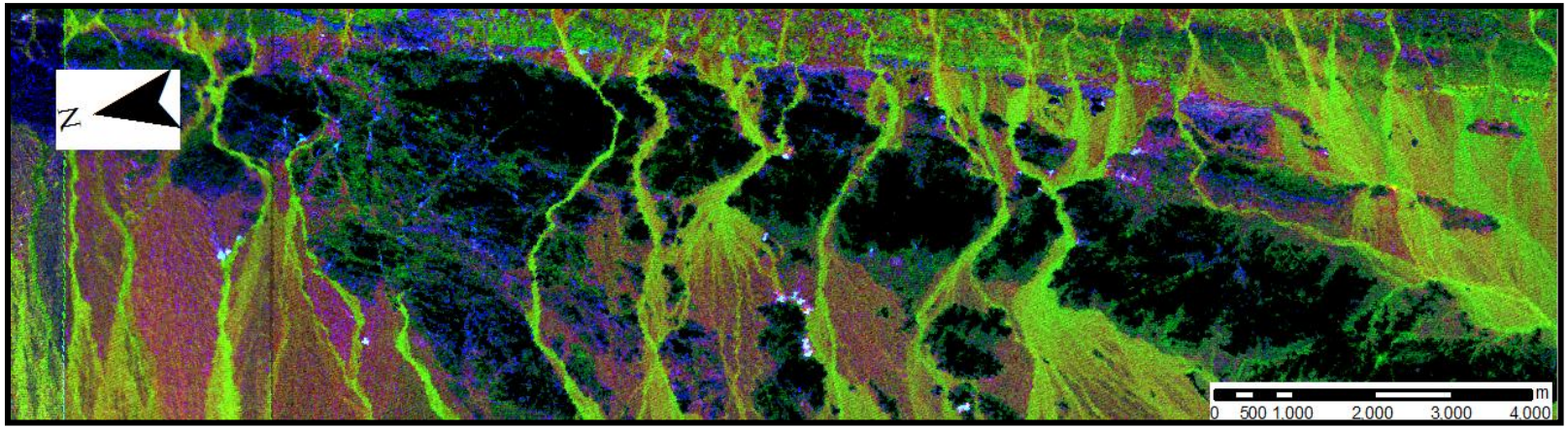

Figure 3.6: Displaced block siliciclastics interspersed with crystalline rocks at the south eastern flank of the Nushki Basin. Note the deflection of the stream and alluvial fans to the right.

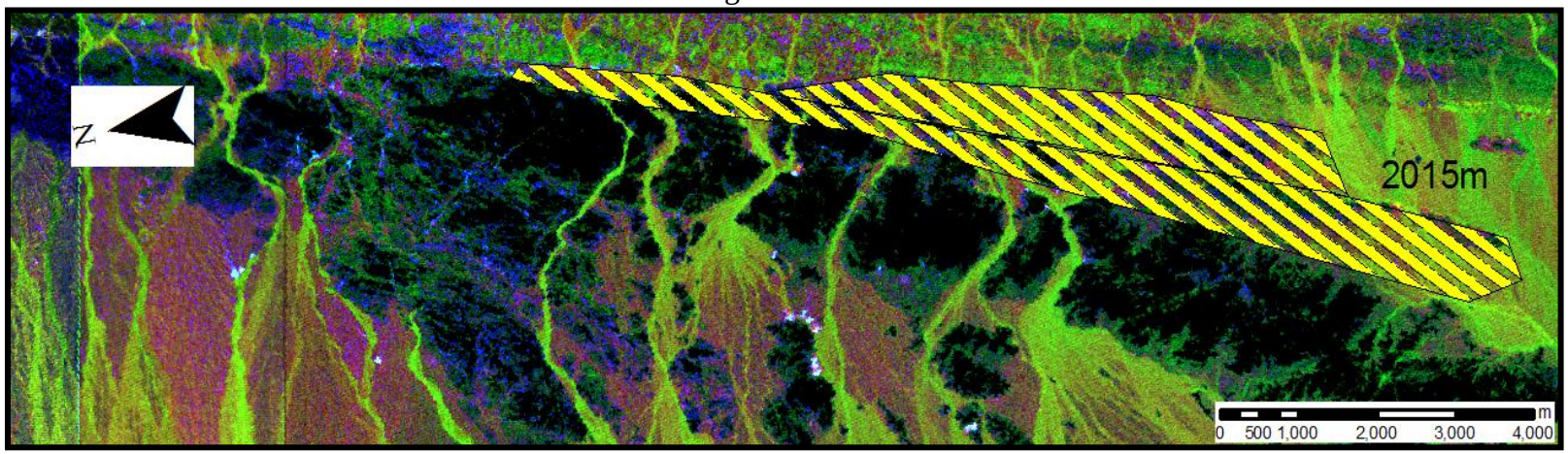

Figure 3.7 below shows a measured displacement of about 2015 meters.

3.3 Ridge Topography

Three distinct ridges have been recognized in the Nushki Basin. The northern ridge and the central ridge are both parts of the Roghani Ridge of Lawrence (1981) and Ul-Hadi et al., (2012) and the southern ridge. The northern and central ridges both belong to the Spinitizha crystalline complex described by Lawrence (1981) and Roghani Ridge of Ul-Hadi et al., (2012). Recent uplift of the Roghani Ridge above the sedimentary strata has altered the local base level of the drainage system (Ul-Hadi, 2012). Highly incised and gently west-sloping alluvial fans surround the ridge from all sides but more predominant in the west. Major direction of stream flow here is E-W.

The northern ridge (Figure 3.2) is dissected by three (2) wind gaps and one corresponding (1) water gap. The two wind gaps correspond to older inactive channels where the deflected stream forming the water gap might have flowed before. The oldest wind gap lies about 2450 m from the water gap with an elevation difference of about 25 m while the younger wind gap lies 1300 m from the water gap with an elevation difference of about 60 m relative to the water gap. Thus it can be inferred that two major episodes of uplift have affected the northern ridge. The first was a 25 m uplift and the second is a

60 m of uplift both leading to the translation and deflection of the antecedent stream for about 2450 m. Also the direction of propagation of vertical uplift in the area is mainly towards the north due to more abundance of wind gaps northwards.

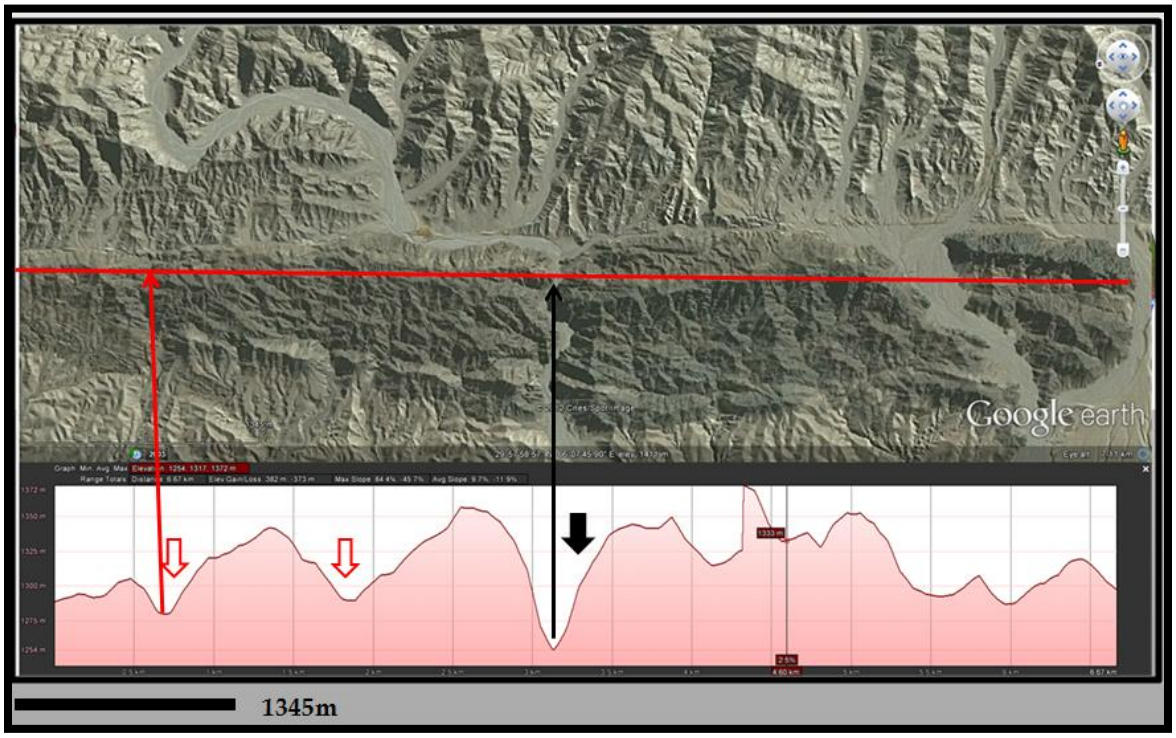

Figure 3.8: Profile along the northern ridge showing three (2) wind gaps (white arrows) and one water gap (black arrow) The northernmost wind gap is about 2450 m from the water gap while the more central wind gap is 1300 m from the water gap.

3.4 Morphometric Analysis

3.4.1 Mountain-front Sinuosity (Smf)

Mountain-front sinuosity (Smf) measurements were taken from the three (3) major mountain fronts making up the Nushki Basin; the northern ridge, the central ridge, and the southern ridge (Figures 3.9A, 3.9 B, and 3.9C respectively). Smf values calculated for the three ridges are 1.25, 1.21, and 1.11 respectively (Table 3.2). These values indicate actively uplifting mountain fronts.

3.4.2 Stream-length Gradient Index (SL)

SL index was calculated for 176 stream reaches from 34 stream segments in the 5 drainage basins making up the Nushki Basin. (Figure 3.10, Figure 3.11, Figure 3.12). The calculated SL index values were interpolated using the Inverse Distance Weighted method (IDW) on ArcGIS (Figure 3.12). The interpolated values were classified into five (5) distinct classes using the equal distance method. Higher values of the SL index suggest recent tectonic activity while low values are characteristically associated with areas of low tectonic influence. SL index can also be dependent on rock lithology as streams flowing across bedrock channels tend to have steeper gradients than streams flowing across alluvial channels (Keller and Pinter, 1996, Coung and Zuchiewicz, 2001, Audin et al., 2006). Thus, abnormal values of the SL index could serve as good indicators of recent uplift. Very low SL index values were recorded along some stream profiles cutting through the crystalline rocks of the Spinitazha crystalline complex on the northern parts of the Roghani ridge. This might have been as a result of gorging caused by shearing in response to fault movement. Thus the gorge acts as a plane of weakness across which the streams flow hence leading to low SL index values (Keller and Pinter, 2002).

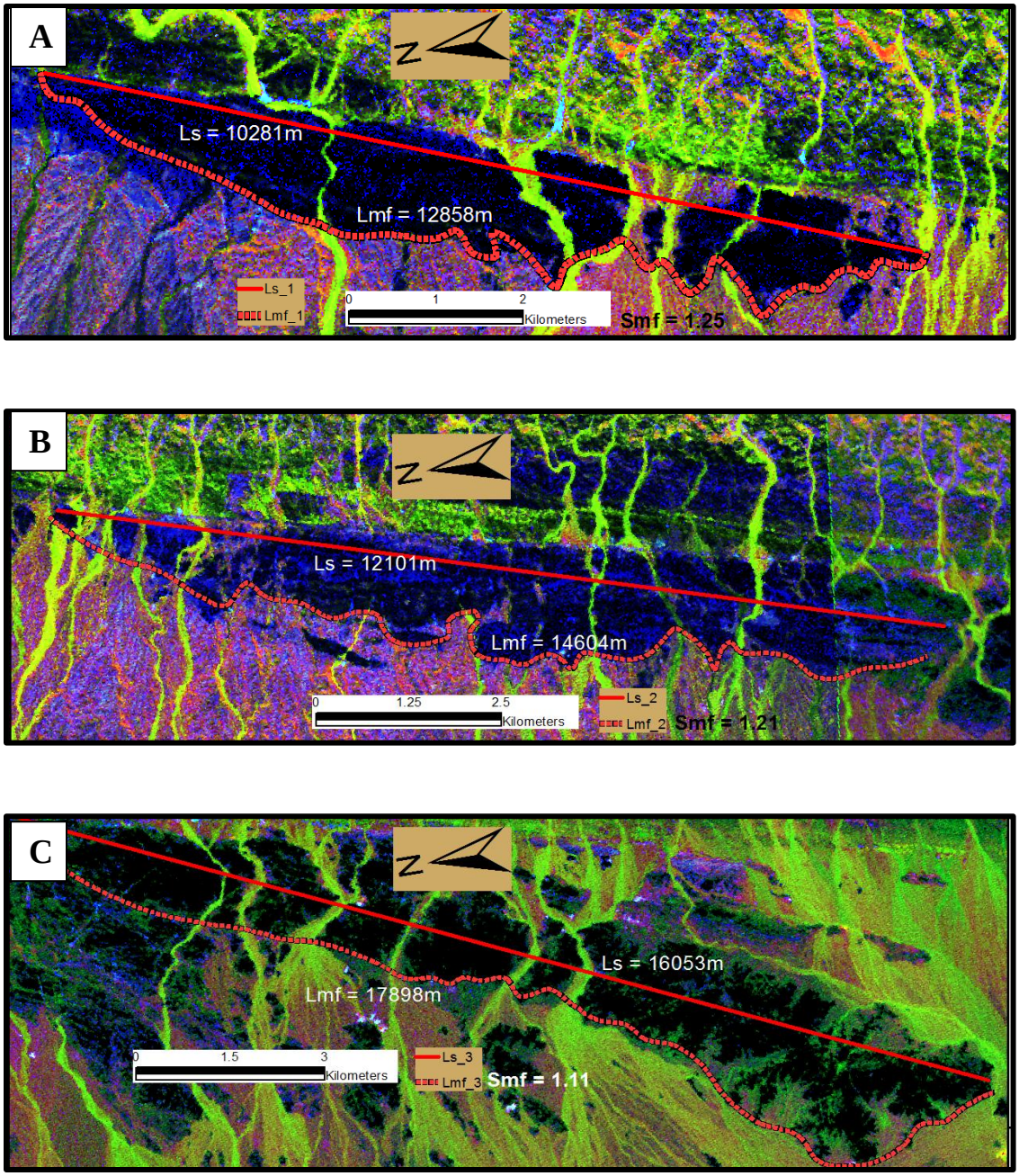

Figures 3.9 (A), 3.9 (B) and 3.9(C): Mountain-front sinuosity (Smf) calculated for three mountain fronts; Northern, Central, and Southern mountain fronts respectively. Smf values here are generally less than 1.5 indicating actively uplifting mountain fronts.

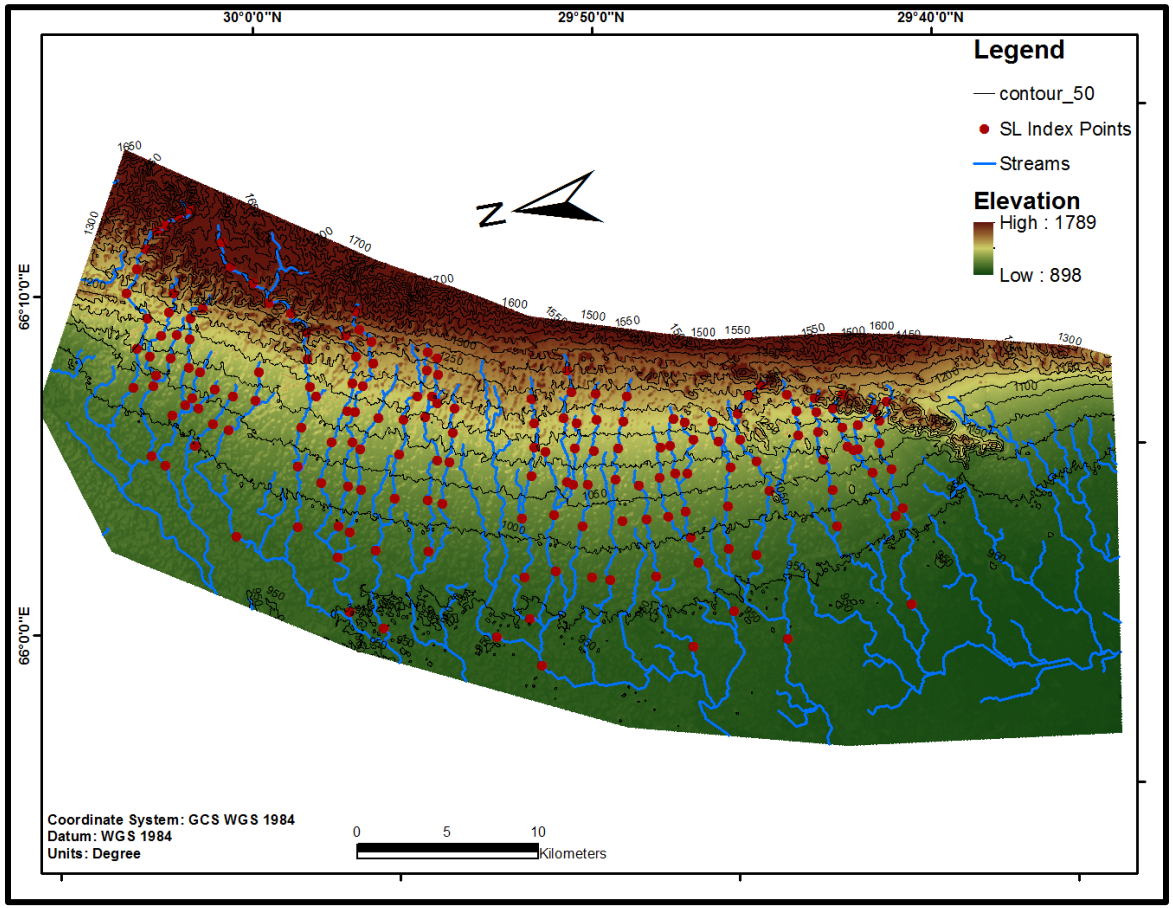

Figure 3.10: 50m elevation contours (black lines) used in calculating SL index. The red dots are points where SL index was calculated while the blue lines are stream networks generated from digital elevation models (DEM)

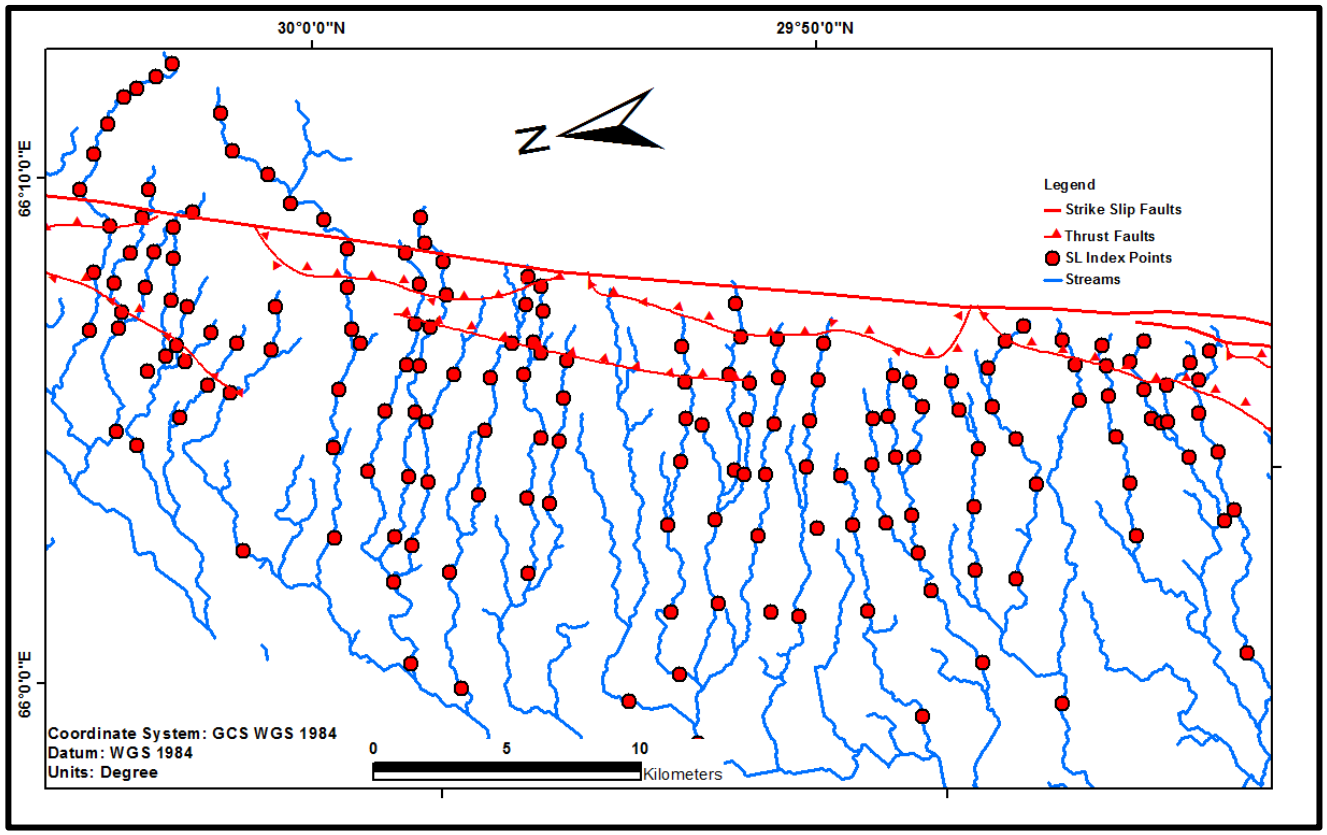

Figure 3.11: Stream network of the Nushki Basin showing points where the SL index was calculated (Red Circle

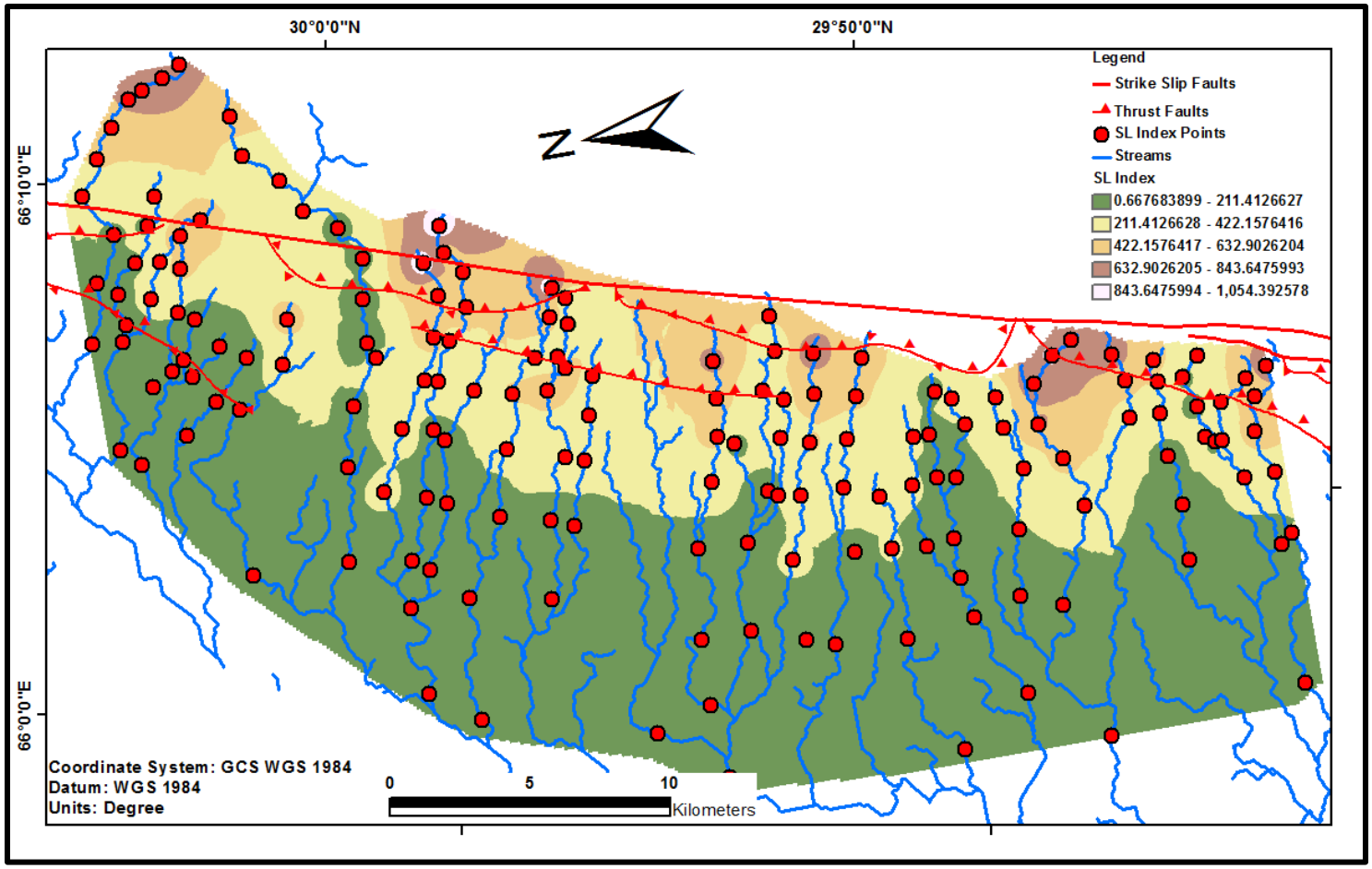

Figure 3.12: Results of IDW interpolation of SL index values. Higher values are found around the major fault lines suggesting a more tectonic control on the SL index values.

Table 3.2 Values used for calculating mountain front sinuosity along three (3) mountain fronts.

Mountain Front	Ls (m)	Lmf (m)	Smf
Northern	10281	12858	1.25
Central	12101	14604	1.21
Southern	16053	17898	1.11

3.4.3 Valley-floor Width to Height Ratio (Vf)

Profiles of eight (8) valleys across the three mountain fronts were measured. (Figure 3.14 A & B). Results show lower Vf values in the central and northern mountain fronts while the southern mountain fronts show a high Vf value (Table 3.3, Figure 3.15). Since low Vf values correlate with areas of high and rapid rate of uplift, these results confirm a northwards direction of propagation of lateral uplift in the Nushki Basin.

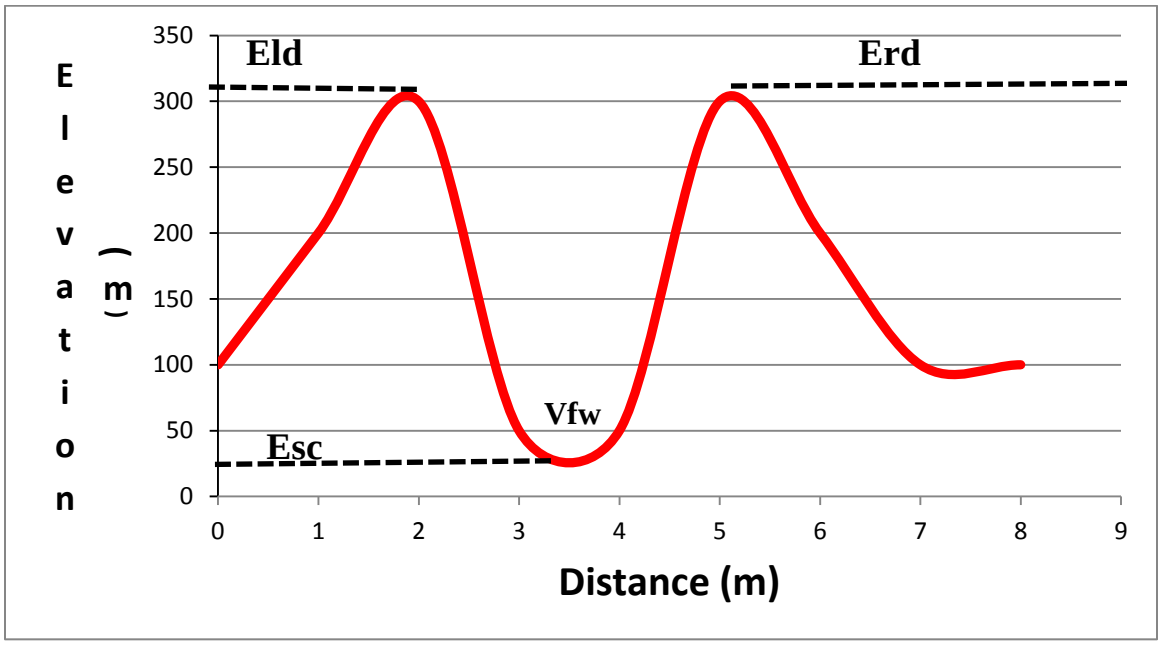

Figure 3.13: Calculating the valley-floor width to height ratio, Vf. (Modified from Keller and Pinter, 2002)

Table 3.3: Data used for calculating Vf values shown in Figure 3.18 (A-H).

S/no	Vfw	2Vfw	Esc	Eld	Erd	(Eld – Esc)	(Erd – Esc)	[(Eld – Erd)] + (Erd – Esc)]	Vf
Vf 1	15	30	1172	1195	1184	23	12	35	0.86
Vf 2	10	20	1209	1217	1209.6	8	0.6	8.6	2.33
Vf 3	40	80	1212	1308	1276	96	64	160	0.5
Vf 4	14	28	1233	1250	1246	17	13	30	0.93
Vf 5	14	28	1278	1292	1291	14	13	27	1.044
Vf 6	20	40	1277	1287	1280.5	10	3.5	13.5	2.96
Vf 7	10	20	1209.2	1216.8	1218	7.6	8.8	16.4	1.22
Vf 8	30	60	1211	1218.5	1223	7.5	12	19.5	3.08

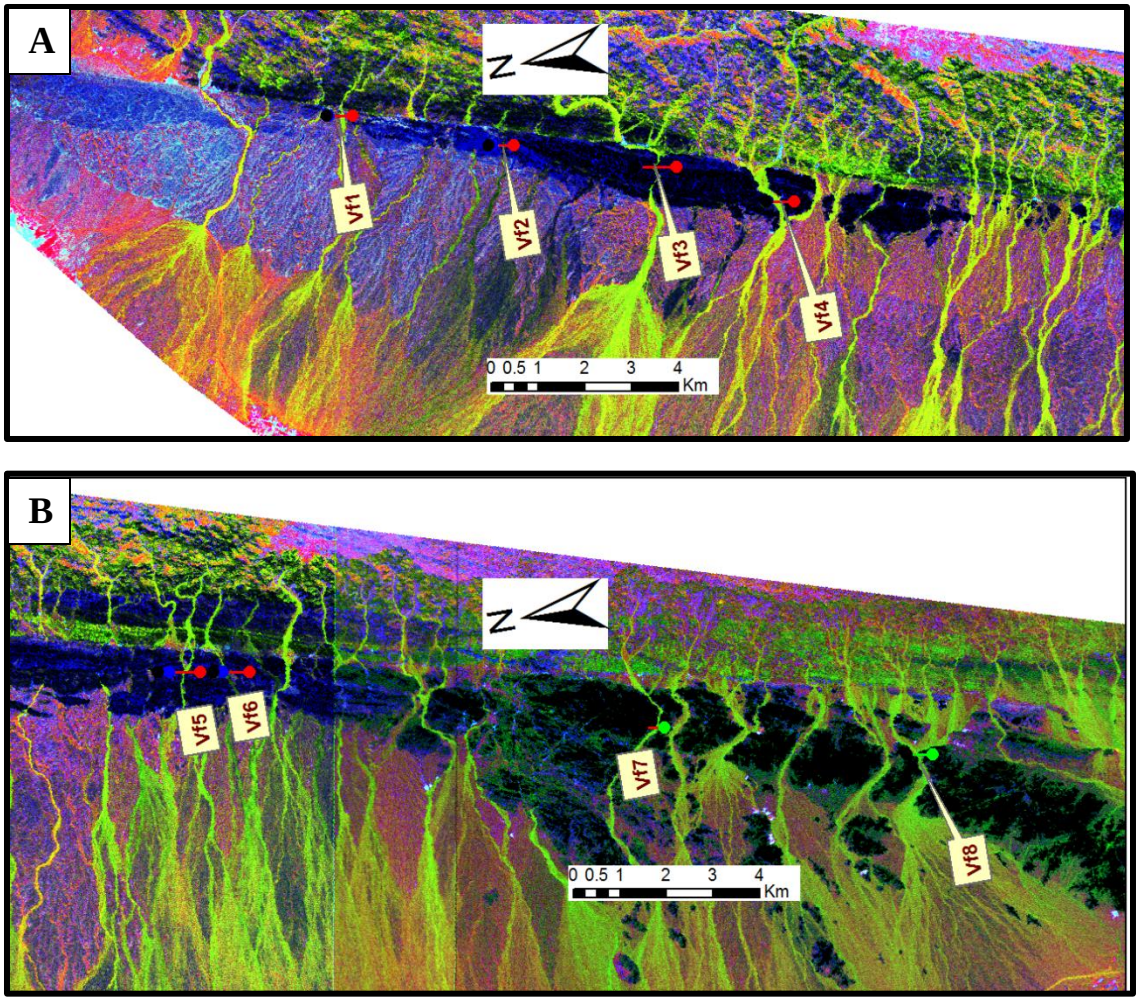

Figures 3.14 (A & B): Points of Vf measurements from the northern mountain front through the southern mountain front. (A) Vf1, Vf2, Vf3, Vf4. (B) Vf5, Vf6, Vf7, Vf8

A)

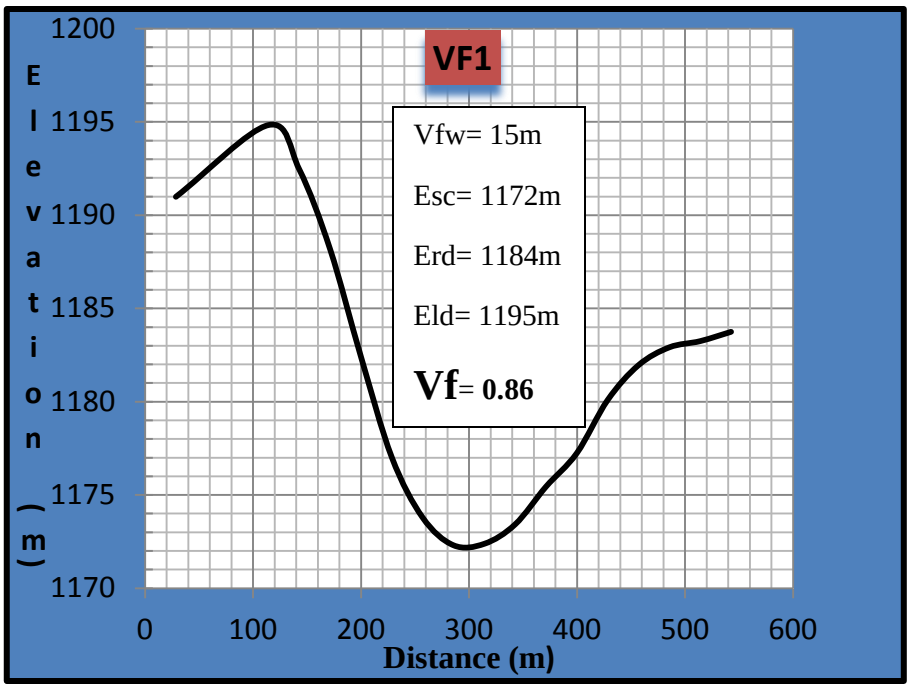

B)

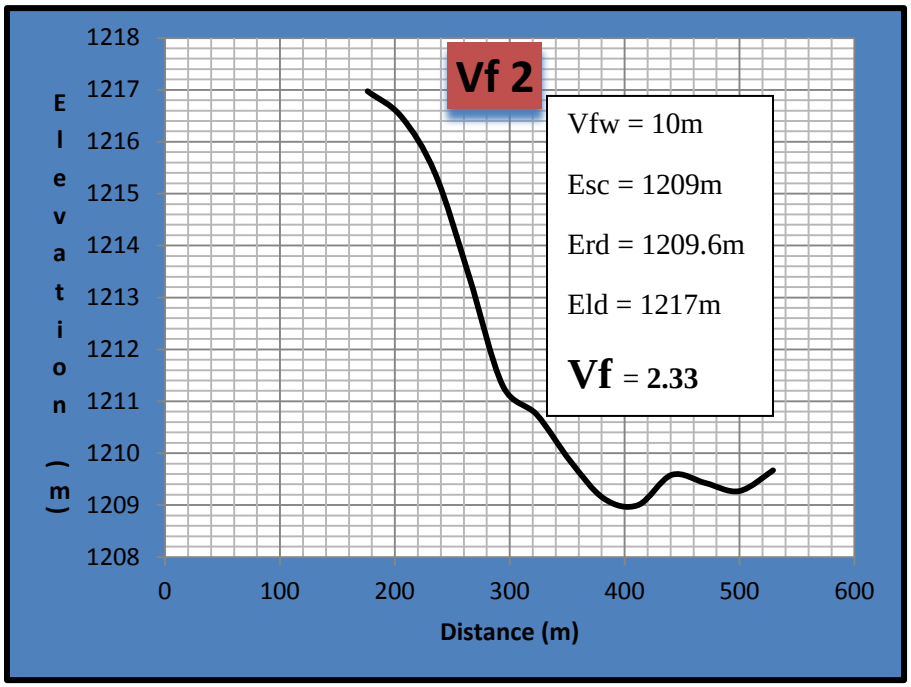

Figure 3.15: (A-H) Valley profiles of 8 valleys used for calculating the Vf ratio from north to south. Note the general decrease in Vf values northwards of the basin. Low Vf values represent areas undergoing rapid uplift. The generally low Vf values in the north shows a northward propagation of uplift in the basin.

C)

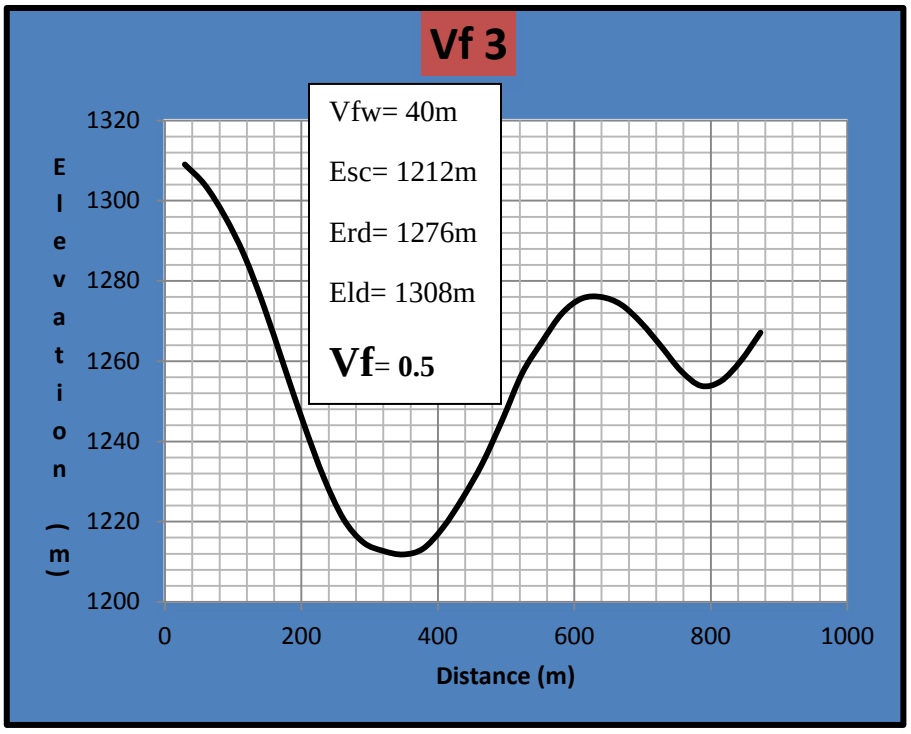

D)

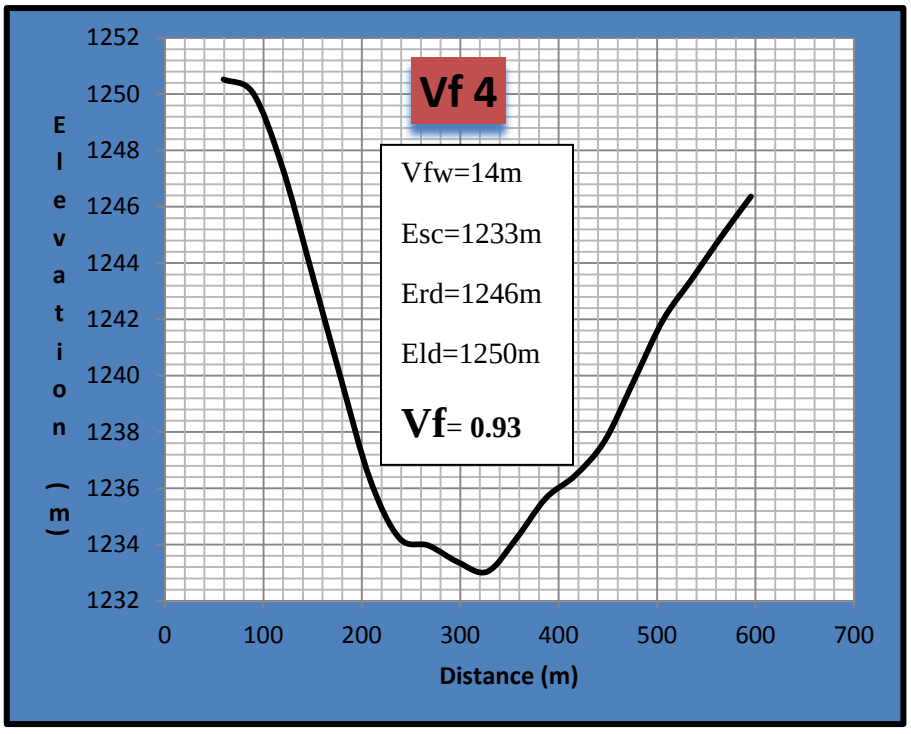

Figure 3.15 continued

E)

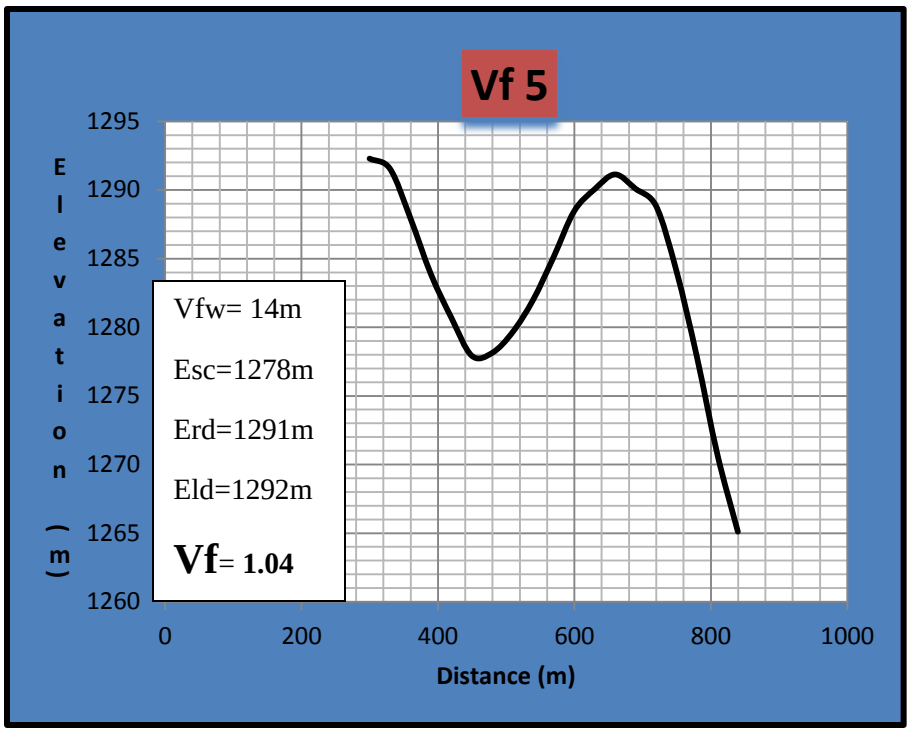

F)

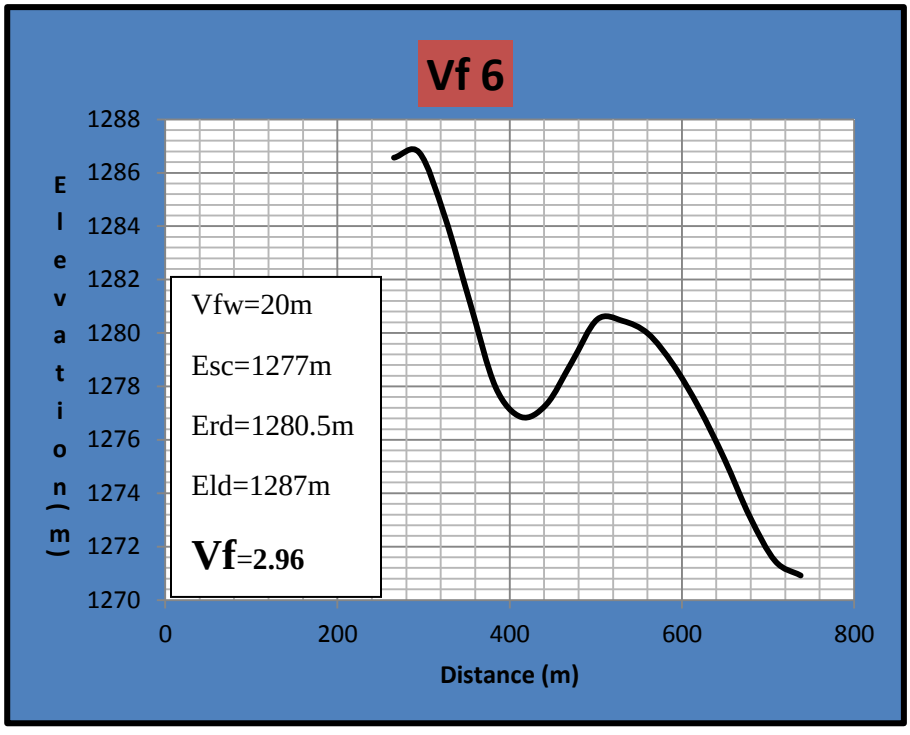

Figure 3.15 continued

G)

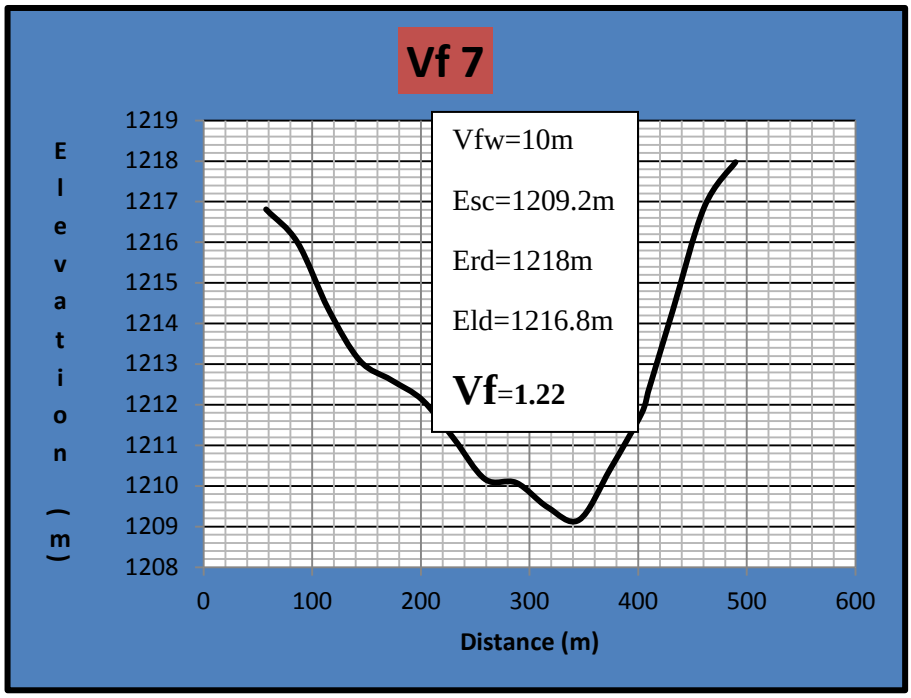

H)

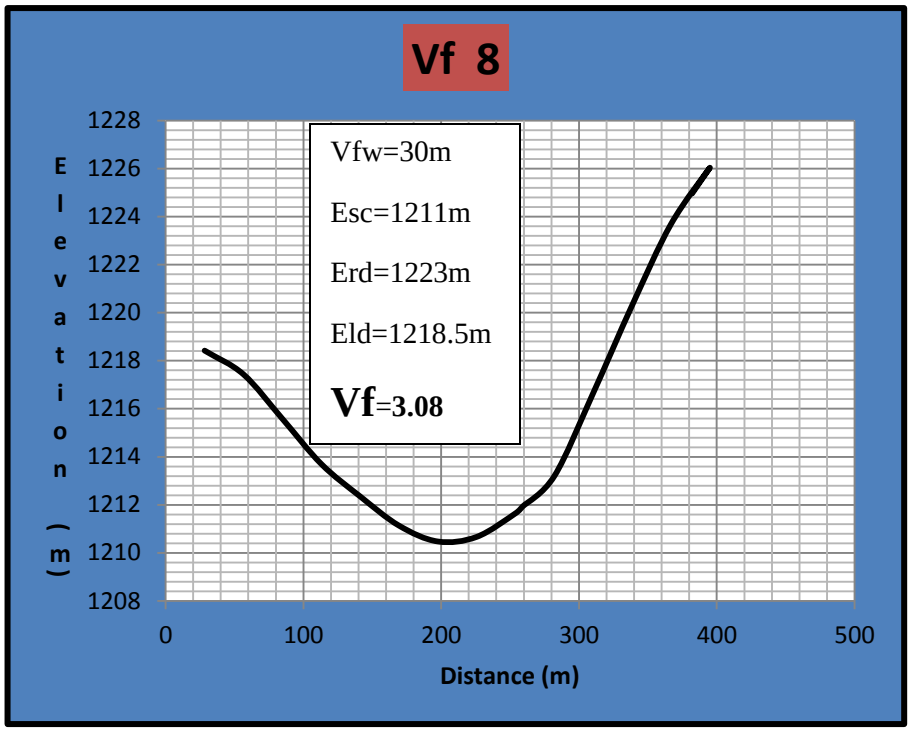

Figure 3.15 continued

CHAPTER 4: DISCUSSION OF RESULTS

Numerous geomorphic expressions of active deformation which characterize transpressive regimes are recorded in the Nushki Basin. These include beheaded streams, stream offsets, fan offsets, deposition style of alluvial fans, uplifted fans, and linear drainage style. The pattern and distribution style could serve as pointers towards the tectonic style of the area. Thus, in order to define a tectonic model for the study area, which is part of an intra-continental collision zone, it is pertinent to understand the relationships between the various geomorphic expressions of active deformation in the area. This has been carried out through measurements of geomorphic indices and measurements of offsets and displacements as discussed in the preceding chapter.

GPS and InSAR studies on different parts of the Chaman fault have yielded slip rates of 18 ± 1 mm/yr (Mohadjer et al., 2010) and a post-seismic slip-rate of ~ 8 mm/yr (Furuya and Satyabala, 2008) respectively. In contrast, Lawrence et al. (1992) provided a geologically constrained displacement of 460 ± 10 km, based on four observed regionally displaced features including: i) presence of a major thrust fault laterally displaced for ~ 250 km on both sides of the Chaman fault; ii) correlation of subduction complexes present on both sides of the fault; iii) the depression of the Kharan desert south of the Ras Koh is equivalent to that of the Ab-e-Istada depression south of the Gardez fault, iv) the sediment of the eastern Makran Ranges is equivalent to the sediment of the Katawaz Basin. These implied an average slip rate of 19 – 24 mm/yr since the inception of the strike-slip motion on the Chaman fault from 25 – 20 Ma (Lawrence et al., 1992). Beun et al. (1979) on the other hand, extrapolated the offset of ~ 60 – 80 km along a north-south

fault in a volcanic unit dated at ~ 2 Ma to the Chaman fault estimating a slip-rate of 25 – 35 mm/yr.

Recent work by Ul-Hadi (2012) based on observations of alluvial fan offset and uplifted ridges along a strand of the Chaman fault just North of Nushki (Figure 3.1) yielded a slip rate of 33.1±3.2 mm/yr (Table 4.1).

Geomorphic indices have been used as indicators of actively deforming zones in active geodynamical settings (Keller and Pinter, 2002; Traoini and Della Seta, 2008; Font et al., 2010). They help to give a clearer picture in defining the impact of differential uplift on drainage systems and mountain fronts in tectonically active settings (Font et al., 2010). The direction of lateral propagation of deformation could also be inferred from careful observation and analysis of the characteristic landforms, drainage patterns, and evolving structure (Ul-Hadi, 2012). Active faults and folds commonly have topography that can assist in identifying different geomorphic or structural segments along a structure, and estimating the potentially most active segments. Discrimination among different geomorphic segments along a structure is facilitated through detailed studies of drainage pattern, coupled with geomorphic indices, with the objective of determining relative intensity of tectonic activity along a fault or fold relative to other areas (Azor et al., 2002; Keller and Pinter, 2002). The distinction between active and less active structures can be achieved through detailed studies of geomorphic indices of active tectonics, for example, stream length gradient index, mountain front sinuosity, valley floor width to height ratios and entrenchment of Quaternary deposits, and coeval drainage pattern that encompass a fault or fold (Keller and Pinter, 2002; Keller and DeVecchio, 2012). A total of four (4)

different geomorphic indices were calculated for the area around the Nushki Basin. These include; i) Stream-length gradient index. ii) Valley -floor width to height ratio, iii) Mountain-front sinuosity, iv) Topographic analysis.

Table 4.1: Previously reported offsets and slip-rates along different segments of the Chaman fault (Modified from Ul-Hadi, 2011)

Slip-rate (mm/yr)	Location	Methods/Features used	Reference
08.0	31.96°N, 67.55°E	InSAR (a Mw 5.0 earthquake, Oct. 21, 2005)	Furuya and Satyabala, 2008
18 ± 1	Northern segment where Chaman fault bifurcates in to two strands	GPS observations over a seven years' time period	Mohadjer et al., 2010
19 – 24	Central segment of the fault from 29° N to 35° N near Chaman	Matching four features displaced along the fault	Lawrence et al., 1992
25 – 35	Northern segment of the fault in Afghanistan	~ 80 km displacement in a 2 Ma old volcanic unit and extrapolating the rate to the Chaman fault	Beun et al., 1979
33.1±3.2	Northern Segment of the fault in Pakistan, just North of Nushki	Alluvial fan offsets, uplifted ridges and, geomorphic indices	Ul Hadi et al., 2012

4.1 Analysis of Geomorphic Indices and Tectonic Implications

Stream-length gradient index results were analyzed along stream profiles throughout the basin to determine the relative amount of active uplift in the area. Interpolated results show predominance of high values of SL in areas around the major fault strands in the

area and SL values begin to decrease as we move westwards away from the major faults irrespective of the lithologies (Figure 3.12). In addition to this general trend in SL index values, lower values are interspersed within regions where high SL values are dominant. Thus, there is a spatial variation in the relative level of uplift in the basin. Tectonic control on the general deformation in the basin is much localized to areas around active strands of the fault as opposed to a much more regional scale. The only recognizable trend observed from SL index result was the tendency of the higher SL values which signifies high uplift rates to coincide with some areas around active fault lines and very low values away from the faults (Figure 4.1).

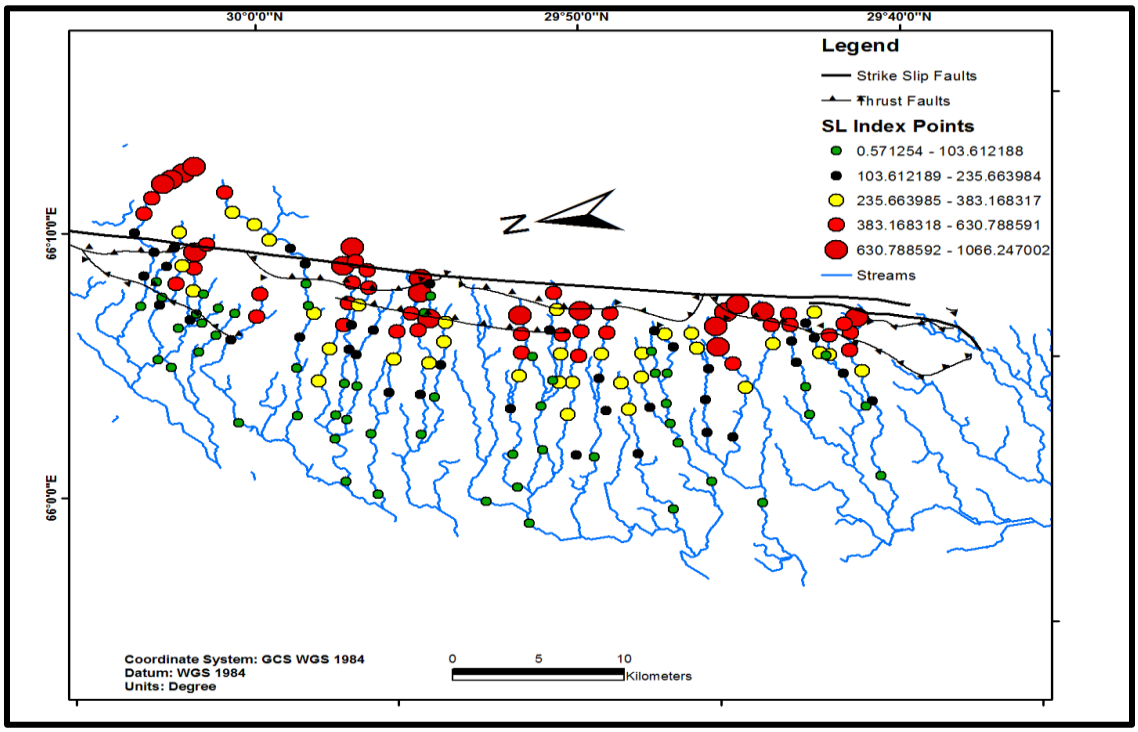

Figure 4.1: Statistical distribution of SL index values measured on 176 stream segments. The Calculated SL index values were classified into 5 distinct groups. The two highest groups of SL values are represented with red circles. The yellow, red, and black circles represent the 3 lowest values. The distribution of high SL index values shows a general clustering of the red circles in close proximity to the fault zone. This pattern shows that the gradients are controlled by active fault movements.

Valley-floor width to height ratio Vf, is a measure of amount of vertical uplift in the basin. Eight (8) valley profiles distributed along the three (3) mountain fronts in the area were used in the calculation. The results show a general increase in the Vf values from north to south. Low Vf values are associated with actively uplifting areas with rapid stream down cutting. The Vf2 which is at the northern flank of the basin shows an abnormally high value of Vf ratio (Figure 4.2). An observation from the satellite image shows that Vf2 is an abandoned channel with no active stream flowing through the channel. Higher values of Vf ratio in the southern flanks of the basin with U-shaped valley profiles suggest an erosion-dominated part of the basin.

Thus, the direction of lateral propagation of uplift as deduced from the Vf ratio is towards the northern flanks of the basin. This is in agreement with the work of Ul-Hadi (2012) who also suggested a northward propagation of lateral uplift in the Chaman Basin, just north of the Nushki Basin.

Mountain-front sinuosity is a measure of predominance of tectonic forces or erosional forces acting on a mountain or ridge. Tectonically active (straight) mountain fronts are characterized by low Smf values usually close to 1, while erosion controlled mountain fronts are characterized by higher Smf values of >1.5.

Results from calculations of the mountain-front sinuosity (Smf) for three mountain fronts in the Basin shows an actively uplifting area around the major strike-slip Chaman fault. The Smf values for the northern, central, and southern ridges are 1.21, 1.25 and 1.11 respectively. These are all in the range of values for actively uplifting mountain fronts as proposed by Keller and Pinter, (2002).

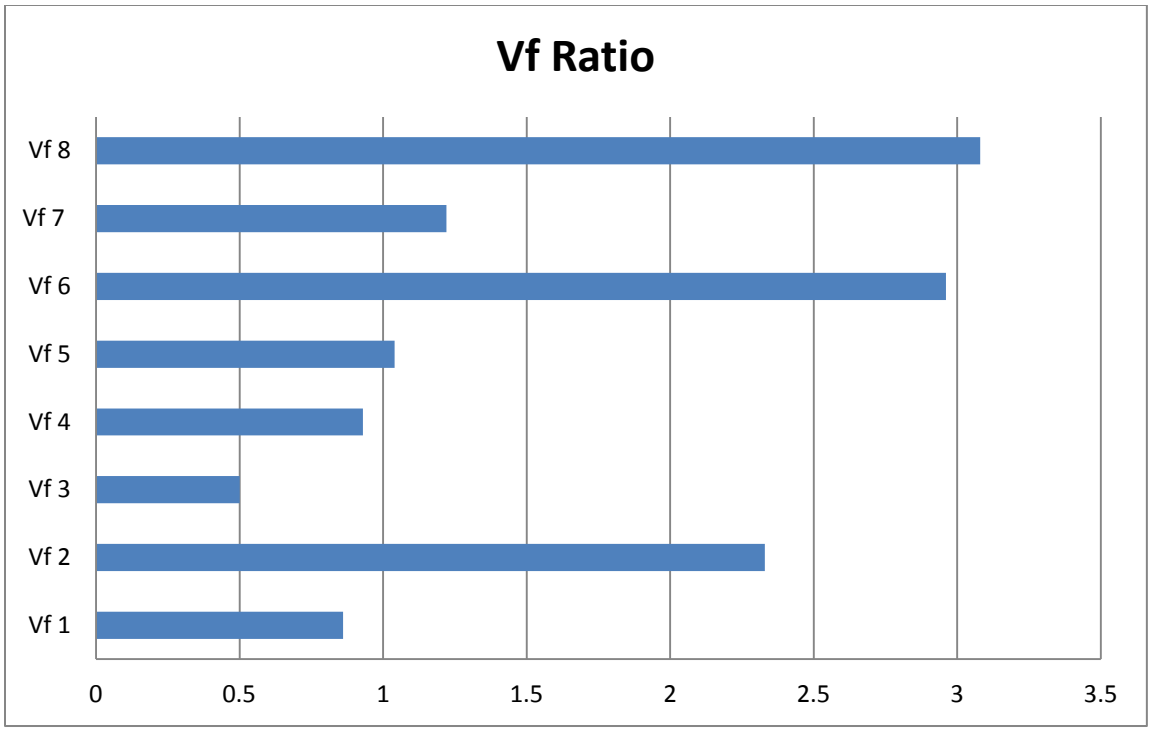

Figure 4.2: Graphic representation of Vf ratio results for eight (8) valley profiles; Vf 1 Vf 8 measured from the northern flank of the Nushki Basin to the southern flank respectively. There is a general increase in Vf values towards the southern parts of the basin. Anomalous values found at Vf 2 and Vf 7 due to stream abandonment and relatively lower erosion rates respectively. In general, the pattern of Vf values shows a northward propagation of the thrust system in the basin.

4.2 Analysis of Offsets/Displacements and Neotectonic Implications

Offsets are commonly associated with strike-slip fault movement. Four offset features were identified on landforms along the different strands of the Chaman strike-slip fault (Figures 3.2, 3.3, 3.5, and 3.6). The offsets all show a left lateral displacement orientation. The amount of measured offsets shows a general increase towards the northern flank of the basin along the main Chaman strike-slip fault. Thus, measured displacement in a N-S orientation on a part of the Roghani Ridge, deflected stream along the Roghani Ridge , ridge located south of the Nushki Basin and, alluvial fan south of the Nushki Basin are 6980 meters, 2384 meters, 2015 meters, and 235 meters respectively.

Hence the effects of active strike-slip movement in the area begin to wane towards the south.

4.3 Analysis of Ridge Topography

The topography of parts of the Roghani Ridge records a history of the deflection for the stream deflected southwards along the ridge (Figures 3.2 and 3.3). A transverse profile along the ridge shows the presence of two wind gaps and a corresponding water gap (Figure 4.3). This might be responsible for the deflection of the stream southwards as the rate of uplift begins to translate towards the northern parts of the Nushki Basin. This pattern of northward translation of uplift is in agreement with the works of Ul-Hadi, 2012 in the Chaman Basin, north of the Nushki Basin

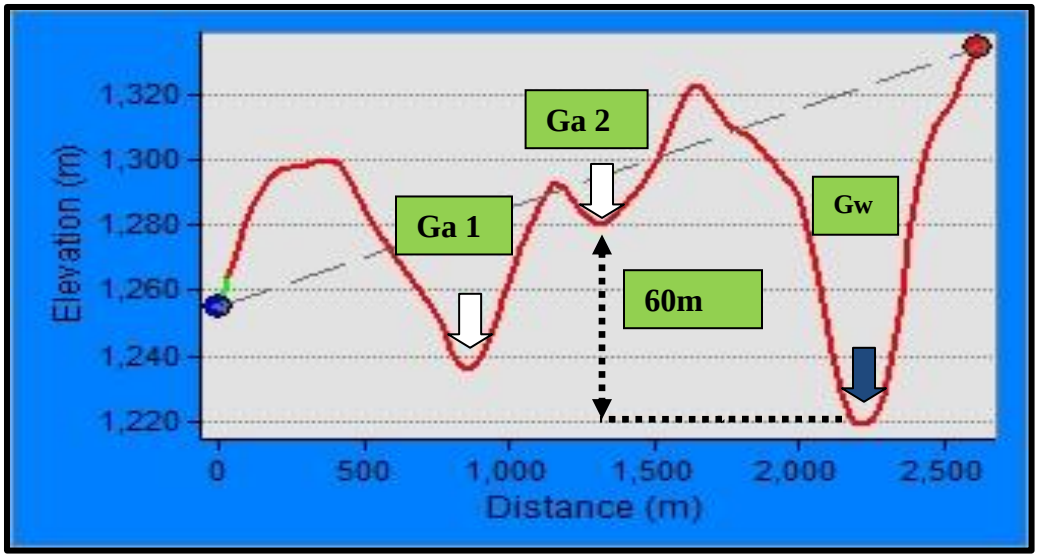

Figure 4.3: Transverse profile in N-S direction along the Roghani Ridge obtained from ASTER image draped over 15 meter resolution DEM. Two wind gaps (Ga1, Ga2, white arrows) and one corresponding water gap (Gw) were identified. Vertical elevation difference of about 60 meters was measured between Ga 2 and the water gap Gw. The profile records the translation of the main antecedent stream (Figure 3.3) due to uplifting of the ridge for about 60 meters. The orientation and distribution of the water gaps relative to the wind gaps suggests a northwards propagation of the thrust which is in agreement with earlier work by Ul-Hadi 2012.

Careful observation of the displacement on the Northern ridge shows a positive flower structure (Figure 4.4). These are upward convex structures with gentle dips which commonly appear as an antiformal area (Harding, 1985). They result from components of convergent movement along the slip plane (Turner, 2001). Thus, they serve as very good examples of structures formed as a result of strike slip and thrust fault interactions. Recent slip and convergence (transpression) of the Indian and Eurasian plates is responsible for the development of this positive flower structure in the Northern ridge. This is further evidence of higher rate of transpression northwards.

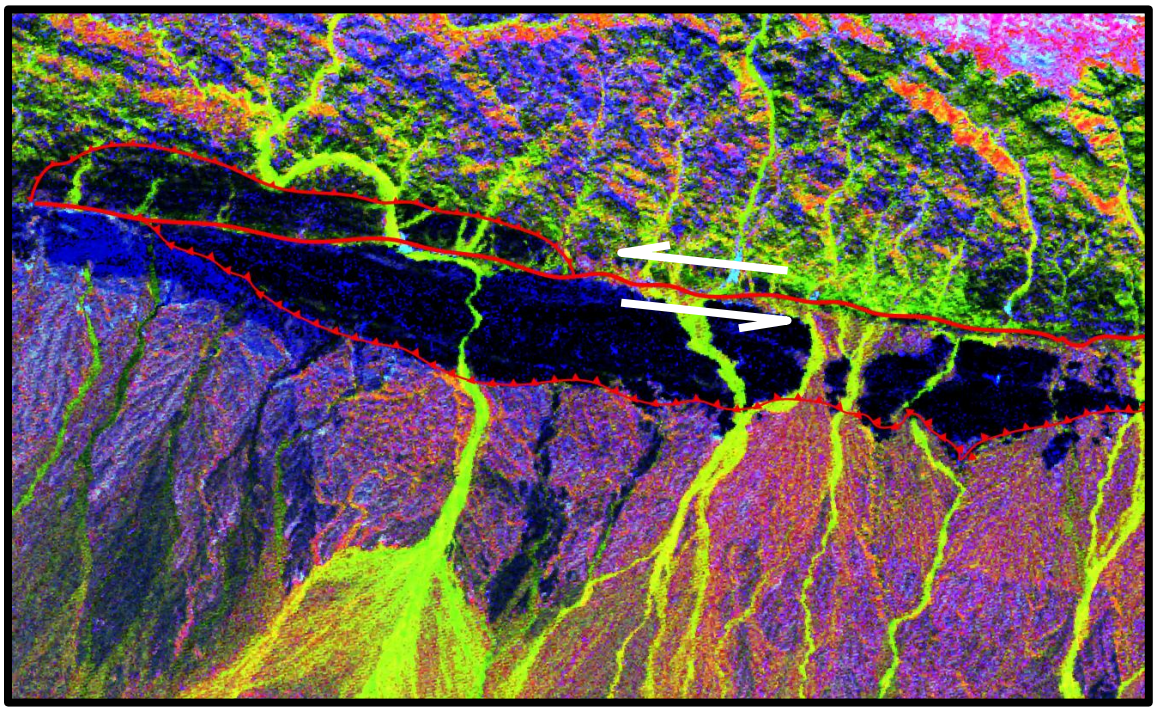

Figure 4.4: Positive flower structure developed on the northern ridge. Both sides of the ridge are bounded by thrust faults. Such structures form in areas with a predominance of strike-slip and thrust fault interaction (transpression).

CHAPTER 5: SUMMARY AND CONCLUSION

Results obtained from analysis of geomorphic indices show strong tectonic controls on landforms in the Nushki Basin. High SL values in areas around the main Chaman strike-slip fault and the thrust faults suggest recent fault movement and uplifts around the faults. The low SL values recorded at the western side of the fault zone suggest lower rates of fault movement and uplift as we move into the gently dipping areas away from the mountain fronts towards the basin.

Analysis of `the valley-floor width to height ratio Vf, mountain-front sinuosity Smf, and topographic profiles all support observations from earlier works of a northern direction of propagation of uplift from transpression.

The measured offsets show varying amounts of displacements. Total displacements in the northern segments are relatively higher than those in the south. This suggests a relatively more tectonically active north compared to the more erosional controlled southern segment. The translation of fault movement mostly towards the northern part of the basin might have been as a result of a higher rate of convergence between the Indian plate and Eurasian plate as suggested by Lawrence, et al. (1981).

Ongoing transpression is responsible for the positive flower structure in the northern ridge. The absence of similar structures in other parts of the basin suggests a higher rate of deformation and propagation of thrusts towards the north of the basin.

BIBLIOGRAPHY

Ambraseys, N., & Bilham, R. (2003). Earthquakes and associated deformation in northern Baluchistan. *Seismological Society of America, 93*, 1573-1605.

Ata, H. (1998). A test of the validity of morphometric analysis in determining tectonic activity from ASTER derived DEMs in the Jordan-Dead Sea transform zone. *PhD Dissertation; University of Arkansas*, 1-238.

Audin, L., David, C., Hall, S., Farber, D., & Herail, G. (2006). Geomorphic evidences of recent tectonic activity in the forearc, Southern Peru. *Revista de la Asociacion Geologica Argentina, 64*(4), 545-554.

Azor, A., Keller, E. A., & Yeats, R. S. (2002). Geomorphic indicators of active fold growth: South Mountain-Oak Ridge anticline, Ventura basin, Southern California. *Geological Society of America Bulletin, 114*(6), 745-753.

Bendick, R., Bilham, R., Freymueller, J., Larson, K., & and Yin, G. (2000). Geodetic evidence for a low slip rate in the AltynTagh fault system. *Nature, 404*, 69-72.

Beun, N. B. (1977). Premières données quantitative relatives' aucoulissage du décrochement de Chaman (Afghanistan du sud-est). *C. R. Acad., 288*, 931-934.

Bull, W. (1977a). Tectonic geomorphology of the Mojave Desert: Menlo Park, California, U.S. *Geological Survey Office of Earthquakes, Volcanoes, and Engineering Contract Report, Contract Rep. 14–08–001-G-394*, 1-188.

Bull, W., & McFadden, L. (1977). Tectonic geomorphology north and south of the Garlock Fault, California, Geomorphology in arid regions. *Geomorphology*, 115-138.

Cuong, N., & Zuchiewicz, W. (2001). Morphotectonic properties of the Lo River Fault near Tam Dao in North Vietnam. *Natural Hazards and Earth System Sciences, 1*, 15-22.

E., Z., Konstantinidi, E., & Koukouvelas, I. K. (2004). Tectonic geomorphology of escarpments: The Case of Kompotades and Nea Anchialos Faults. *Bulletin of the Geological Society of Greece, 36*, 1716-1725.

England, P., & Houseman, G. (1986). Finite strain calculations of continental deformation: 2. Comparison with the India–Asia collision zone. *Journal of Geophysical Research, 91*, 3664-3676.

Farah, A., & DeJong, K. (n.d.). Geodynamics of Pakistan. *Geological Survey of Pakistan*, 305-317.

Farhoudi, G., & Karig, D. E. (1977). Makran of Iran and Pakistan as an active arc system. *Geology, 5*, 664-668.

Font, M., Amorese, D., & Lagarde, J. (2010). DEM and GIS Analysis of the stream gradient index to evaluate active tectonics: The Normandy intraplate area (NW France). *Geomorphology, 119*, 172-180.

Furuya, M., & and Satyabala, S. (2008). Slow earthquake in Afghanistan detected by InSAR. *Geophysical Research Letters, 35*(doi: 10.1029/2007GL033049).

Hack, J. (1973). Stream-profile analysis and stream-gradient index. *U.S. Geological Survey Journal of Research, 1*, 421-429.

Harding, T. (1985). Seismic characteristics and identification of negative flower structures, positive flower structures, and positive structural inversion. *Bulletin of the American Association of Petroleum Geologists, 69 (4)*, 582-600.

Howard, A. D. (1967). Drainage analysis in geologic interpretation: A summation. *AAPG Bulletin, 51*, 2246-2259.

Jacob, K., & Quittmeyer, R. (1979). The Makran region of Pakistan and Iran: Trench-arc system with active plate subduction. *Geodyanamics*, 305-317.

Keller, E., & DeVecchio, D. (2012). Tectonic Geomorphology of active folding and development of transvers drainage. *Treatise on Geomorphology (In press)*.

Keller, E., & Pinter, N. (2002). *Active tectonics: Earthquakes, uplift, and landscape* (Second Edition ed.). Englewood Cliffs, New Jersey: Prentice Hall.

Khan, M. (2008). Chaman Fault System (CFS) – A prominent seismo-tectonic feature in Pakistan. *Newsletter of the Cowasgee Earthquake Study Center Department of Civil Engineering, Ned University of Science & Technology, Pakistan, 8* (1), 1-4.

Khan, S., & Mahmood, K. (2008). The application of remote sensing techniques to the study of ophiolites. *Earth Science Reviews, 89*, 135-143.

Lawrence, R., Khan, S., & and Nakata, T. (1992). Chaman fault, Pakistan-Afghanistan. In: Bucknam, R.C., Hancock, P.L., (eds.), Major active faults of the world-Results of IGCP project 206. *Supplement to Annnales Tectonicae, 6*, 196-223.

Lawrence, R., Yeats, R., Khan, S., Subhani, A., & Bonelli, D. (1981). Crystalline rocks of the Spinatizha area, Pakistan. *Journal of Structural Geology, 3*, 449-457.

Meade, B. (2007). Present-day kinematics at the India-Asia collision zone. *Geology, 35*, 81-84.

Mohadjer, S., Bendick, R., Ischuk, A., Kuzikov, S., Kostuk, A., Saydullaev, U., . . . Zubovich, A. (2010). Partitioning of India-Eurasia convergence in the Pamir-Hindu Kush from GPS measurements. *Geophysical Research Letters, 27(*doi: 10.1029/2009GL041737).

Peltzer, G., & Saucier, F. (1996). Present-day kinematics of Asia derived from geologic fault rates. *Journal of Geophysical Research, 101*, 27943-27956.

Peters, G., & van Balen, R. (2009). Tectonic geomorphology of the northern Upper Rhine Graben, Germany. *Global and Planetary Change, 58*, 310-334.

Pidwirny, M. (2006). "The Drainage Basin Concept". In *Fundamentals of Physical Geography* (2nd ed.).

Quittmeyer, R., & Kafka, A. (1984). Constraints on plate motions in southern Pakistan and the Northern Arabian Sea from the focal mechanisms of small earthquakes. *Journal of Geophysical Research, 89*(B4), 2444–2458.

Ramirez-Herrera, M. (1998). Geomorphic Assessment of active tectonics in the Acambay graben, Mexican volcanic belt. *Earth Surface Processes and Landforms., 23*, 317-332.

Ruleman, C., Crone, A., Machette, M., Haller, K., & Rukstales, K. (2007). Map and database of probable and possible Quaternary faults in Afghanistan. *U.S. Geological Survey Open-File Report*, 39p.

Sarwar, G., & DeJong, K. (1979). Arcs, oroclines, syntaxis: the curvatures of mountainbelts in Pakistan. *in Farah, A., and DeJong K. A., eds., Geodynamics of Pakistan:Quetta, Pakistan, Geological Survey of Pakistan*, 351-358.

Szeliga, W., Bilham, R., Schelling, D., Kakar, D., & Lodi, S. (2009). Fold and thrust partitioning in a contracting fold belt: Insights from the 1931 Mach earthquake in Baluchistan. *Tectonics, 28*, doi: 10.1029/2008TC002265.

Tapponnier, P., Xu, Z., Roger, F., Meyer, B., Arnaud, N., Wittlinger, G., & Yang, J. (n.d.). Oblique stepwise rise and growth of the Tibet Plateau. *Science, 294*, 1671-1677.

Tarboton, D. G., Bras, R. L., & Rodriguez-Iturbe., I. (n.d.). On the extraction of channel networks from digital elevation data. *Hydrological Processes, 5*, 81-100.

Thatcher, W. (n.d.). Micro-plate model for the present-day deformation of Tibet. *Journal of Geophysical Research, 112*, doi: 10.1029/2005JB004244.

Troiani, F., & Della Seta, M. (2008). The use of the stream-length gradients index in morphotectonic analysis of small catchments: A case study from Central Italy. *Geomorphology, 102*, 159-168.

Tsoudoulous, I., Ioannis, K. K., & Pavlides, S. (2008). Tectonic geomorphology of easternmost extension of the gulf of Corinth (Beotia, Central Greece). *Tectonophysics, 453*, 211-232.

Turner, J. R. (2001). Evidence for Strike-Slip Faulting in the Smackover Formation of Northeast. *Gulf coast association of geological societies transactions.*, 339-348.

Ul-Hadi, S. (2012). Multidisciplinary investigations of the Chaman strike-slip fault along the western Indo-Asian collision boundary, Pakistan. *PhD Dissertation: University of Houston*.

Ul-Hadi, S., Khan, S., Owen, L., & Khan, A. (2012). Geomorphic response to an active transpressive regime: a case study along the Chaman strike-slip fault, western Pakistan. *Earth Surface Processes and Landforms.*, DOI: 10.1002/esp.3272.

Yamaguchi, Y., Kahle, A. B., Tsu, H., Kawakami, T., & Pniel, M. (1998). Overview of Advanced Spaceborne Thermal Emission and Reflection Radiometer (ASTER). *IEEE Transaction on Geoscience and Remote Sensing, 36*(4), 1062-1071.

Zhang, P., Molnar, P., & and Xu, X. (2007). Late Quaternary and present-day rates of slip along the Altyn Tagh Fault, northern margin of the Tibetan Plateau. *Tectonics, 26*, doi: 10.1029/2006TC002014.

APPENDIX: Parameters for Calculating Vf Index.

S/no	Length of Reach (ΔL)	Mid point	Longitude	Latitude	Max Contour	Min Contour	Gradient (ΔH)	Upstream Length (L)	SL Index
Basin 1 Stream 1									
1	1131	566	66.197	30.047	1500	1450	50	15397	681
2	879	440	66.194	30.053	1450	1400	50	14392	819
3	939	470	66.191	30.06	1400	1350	50	13483	718
4	930	465	66.189	30.065	1350	1300	50	12548	675
5	1287	644	66.181	30.072	1300	1250	50	11440	444
6	1158	579	66.172	30.078	1250	1200	50	10217	441
7	1687	844	66.161	30.085	1200	1150	50	7108	211
8	1866	933	66.147	30.077	1150	1100	50	6839	183
9	1774	887	66.133	30.085	1100	1050	50	5198	147
10	2405	1203	66.114	30.09	1050	1000	50	3109	65
Basin 1 Stream 2									
1	1032	516	66.157	30.062	1250	1200	50	6412	311
2	1672	836	66.148	30.066	1200	1150	50	5060	151
3	1235	618	66.137	30.072	1150	1100	50	3607	146
4	1634	817	66.128	30.079	1100	1050	50	2172	66
5	942	471	66.118	30.078	1050	1030	20	884	19
Basin 1 Stream 3									
1	1457	729	66.136	30.064	1150	1100	50	10852	372
2	1195	598	66.125	30.069	1100	1050	50	9526	399
3	2717	1359	66.113	30.08	1050	1000	50	7570	139
4	5838	2919	66.079	30.087	1000	969	31	3293	17
Basin 1 Stream 4									
1	1412	706	66.147	30.049	1250	1200	50	13138	465
2	878	439	66.143	30.056	1200	1150	50	11993	683
3	1084	542	66.133	30.058	1150	1100	50	11012	508
4	1974	987	66.119	30.061	1100	1050	50	9483	240
5	2232	1116	66.101	30.066	1050	1000	50	7380	165
6	6086	3043	66.073	30.081	1000	967	33	3221	17
Basin 1 Stream 4B									
1	1867	934	66.116	30.056	1100	1050	50	2384	64
2	1006	503	66.104	30.062	1050	1025	25	948	24

Appendix (Continued)

S/no	Length of Reach (ΔL)	Mid Point	Longitude	Latitude	Max Contour	Min Contour	Gradient (ΔH)	Upstream Length (L)	SL Index
1	1045	523	66.106	30.05	1078	1050	28	2478	66
2	1942	971	66.098	30.06	1050	1025	25	985	13
Basin 1 Stream 5									
1	8884	4442	66.097	30.073	996	951	45	4442	23
Basin 1 Stream 5B									
1	1444	722	66.101	30.042	1086	1050	36	4156	104
2	2353	1178	66.089	30.054	1050	1000	50	2256	48
3	1100	550	66.08	30.065	1000	981	19	531	9
Basin 2 Stream 1									
1	1119	560	66.111	30.027	1135	1100	35	17526	548
2	2002	1001	66.097	30.031	1100	1050	50	15965	399
3	3256	1628	66.085	30.047	1050	1000	50	13336	205
4	11797	5899	66.032	30.052	1000	953	47	5810	23
Basin 2 Stream 2									
1	1192	596	66.178	30.034	1500	1450	50	12035	505
2	1618	809	66.165	30.032	1450	1400	50	10630	328
3	1575	788	66.155	30.022	1400	1350	50	9034	287
4	1460	730	66.144	30.016	1350	1300	50	7516	257
5	1931	966	66.137	30.006	1300	1250	50	5821	151
6	1403	702	66.126	30	1250	1200	50	4154	148
7	1567	784	66.113	30.002	1200	1150	50	2669	85
8	1573	787	66.099	30.003	1150	1100	50	1099	35
Basin 2 Stream 2B									
1	1450	725	66.094	30.001	1140	1100	40	9660	266
2	2170	1085	66.08	30.011	1100	1050	50	7850	181
3	2830	1415	66.061	30.016	1050	1000	50	5350	95
4	3930	1965	66.031	30.021	1000	956	44	1970	22
Basin 2 Stream 3									
1	880	440	66.121	29.981	1300	1250	50	18396	1045
2	1760	880	66.11	29.978	1250	1200	50	17076	485
3	1346	673	66.097	29.982	1200	1150	50	15523	577
4	1756	878	66.084	29.987	1150	1100	50	13972	398
5	1930	965	66.07	29.997	1100	1050	50	12129	314
6	2745	1373	66.051	30.006	1050	1000	50	17464	318
7	7490	3745	66.013	30.004	1000	950	50	4674	31

Appendix (Continued)

S/no	Length of Reach (ΔL)	Mid point	Longitude	Latitude	Max Contour	Min Contour	Gradient (ΔH)	Upstream Length (L)	SL Index
Basin 2 Stream 3B									
1	697	349	66.132	29.974	1400	1350	50	14261	1023
2	1239	620	66.123	29.974	1350	1300	50	13293	536
3	992	496	66.116	29.969	1300	1250	50	12177	614
4	1348	674	66.105	29.97	1250	1200	50	11007	408
5	1406	703	66.095	29.977	1200	1150	50	9630	342
6	1724	862	66.083	29.983	1150	1100	50	8065	234
7	2096	1048	66.068	29.987	1100	1050	50	6155	147
8	2822	1411	66.047	29.993	1050	1000	50	3696	65
9	2169	1085	66.028	30.001	1000	963	37	1201	20
Basin 2 Stream 3C									
1	1986	993	66.078	29.972	1150	1100	50	8458	213
2	1884	942	66.064	29.984	1100	1050	50	6523	173
3	2410	1205	66.044	29.987	1050	1000	50	4376	91
4	2576	1288	66.024	29.996	1000	962	38	1883	28
Basin 2 Stream 4									
1	834	417	66.106	29.942	1300	1250	50	17785	1066
2	1279	640	66.097	29.944	1250	1200	50	16729	654
3	1779	890	66.085	29.951	1200	1150	50	15200	427
4	1516	758	66.075	29.96	1150	1100	50	13552	447
5	2314	1157	66.058	29.965	1100	1050	50	11637	251
6	2421	1211	66.037	29.971	1050	1000	50	9270	191
7	4904	2452	66.013	29.985	1000	950	50	5607	57
8	2321	1161	65.974	29.988	950	7	43	1994	37
Basin 3 Stream 1									
1	469	235	66.102	29.938	1276	1250	26	2874	159
2	1140	570	66.094	29.939	1250	1200	50	2069	91
3	1492	746	66.084	29.944	1200	1154	46	753	23
Basin 3 Stream 1B									
1	1500	750	66.08	29.942	1200	1150	50	10866	724
2	1706	853	66.074	29.949	1150	1100	50	9263	543
3	2382	1191	66.052	29.947	1100	1050	50	7219	303
4	2676	1338	66.033	29.955	1050	1000	50	4690	175

Appendix (Continued)

S/no	Length of Reach (ΔL)	Mid point	Longitude	Latitude	Max Contour	Min Contour	Gradient (ΔH)	Upstream Length (L)	SL Index
5	3262	1631	66.008	29.959	1000	959	41	1721	43
Basin 3 Stream 2									
1	1487	744	66.076	29.934	1200	1150	50	9621	323
2	1294	647	66.064	29.937	1150	1100	50	8230	318
3	1988	994	66.05	29.941	1100	1050	50	9370	236
4	2590	1475	66.03	29.948	1050	1000	50	4120	80
5	5333	2667	65.96	29.933	950	941	9	339	1
Basin 3 Stream 3									
1	1080	540	66.074	29.895	1250	1200	50	15357	711
2	1421	711	66.062	29.896	1200	1150	50	14107	496
3	1337	669	66.05	29.898	1150	1100	50	15229	570
4	1979	990	66.036	29.902	1100	1050	50	11070	280
5	2509	1255	66.016	29.91	1050	1000	50	8826	176
6	4875	2438	65.987	29.914	1000	950	50	5134	53
7	2154	1077	65.966	29.915	950	941	9	1619	7
Basin 3 Stream 4									
1	906	453	66.085	29.875	1300	1250	50	7653	422
2	1234	617	66.074	29.875	1250	1200	50	6583	267
3	1775	888	66.062	29.881	1200	1150	50	5079	143
4	1772	886	66.047	29.893	1150	1100	50	3305	93
5	1651	826	66.03	29.885	1100	1050	50	1594	48
Basin 3 Stream 4B									
1	827	414	66.058	29.875	1180	1150	30	11496	417
2	2032	1016	66.046	29.878	1150	1100	50	10066	248
3	1692	846	66.028	29.882	1100	1050	50	8204	242
4	2556	1278	66.015	29.894	1050	1000	50	3524	69
5	3761	1881	65.987	29.898	1000	950	50	2922	39
Basin 3 Stream 5									
1	1132	566	66.071	29.863	1250	1200	50	19524	862
2	1610	805	66.058	29.865	1200	1150	50	18153	564
3	1761	881	66.043	29.869	1150	1100	50	16468	468
4	2262	1131	66.027	29.875	1100	1050	50	14456	320
5	2335	1168	66.007	29.881	1050	1000	50	12158	260
6	3831	1916	65.981	29.881	1000	950	50	9075	118
7	7002	3501	65.942	29.913	950	935	15	3658	8

Appendix (Continued)

S/no	Length of Reach (ΔL)	Mid point	Longitude	Latitude	Max Contour	Min Contour	Gradient (ΔH)	Upstream Length (L)	SL Index
Basin 3 Stream 6									
1	1381	691	66.067	29.848	1250	1200	50	13071	473
2	1335	668	66.055	29.852	1200	1150	50	11713	439
3	1620	810	66.042	29.857	1150	1100	50	10235	316
4	2102	1051	66.027	29.861	1100	1050	50	8374	199
5	2552	1276	66.006	29.861	1050	1000	50	6047	118
6	3786	1893	65.978	29.872	1000	950	50	2878	38
Basin 3 Stream 7									
1	1818	909	66.022	29.85	1100	1050	50	13932	383
2	2457	1229	66.005	29.849	1050	1000	50	11795	240
3	3636	1818	65.976	29.849	1000	950	50	8748	120
4	6929	3465	65.938	29.837	950	926	24	3466	12
Basin 3 Stream 8									
1	1663	832	66.039	29.836	1150	1100	50	12366	372
2	1746	873	66.024	29.839	1100	1050	50	10661	305
3	2647	1324	66.004	29.838	1050	1000	50	8465	160
4	4122	2061	65.979	29.827	1000	950	50	5080	62
5	2724	1362	65.952	29.814	950	935	15	1657	9
Basin 3 Stream 8B									
1	1198	599	66.052	29.827	1200	1150	50	3562	149
2	1650	825	66.039	29.831	1150	1100	50	2138	65
3	1310	655	66.025	29.831	1100	1059	41	658	21
Basin 3 Stream 8C									
1	701	351	66.049	29.822	1180	1150	30	7375	316
2	1559	780	66.04	29.819	1150	1100	50	6245	200
3	2497	1249	66.024	29.825	1100	1050	50	4217	84
4	2416	1208	66.005	29.829	1050	1000	50	1760	36
5	547	274	65.992	29.829	1000	992	8	279	4
Basin 4 Stream 1									
1	1072	536	66.047	29.808	1187	1150	37	8597	297
2	1247	624	66.037	29.807	1150	1100	50	8510	341
3	2071	1036	66.023	29.803	1100	1050	50	8098	195
4	1925	963	66.004	29.808	1050	1000	50	8171	212
5	2818	1409	65.983	29.811	1000	958	42	7724	115

Appendix (Continued)

S/no	Length of Reach (ΔL)	Mid point	Longitude	Latitude	Max Contour	Min Contour	Gradient (ΔH)	Upstream Length (L)	SL Index
Basin 4 Stream 2									
1	581	291	66.061	29.781	1269	1250	19	21915	717
2	1176	588	66.057	29.788	1250	1200	50	21036	894
3	1238	619	66.049	29.795	1200	1150	50	19829	801
4	1362	681	66.036	29.796	1150	1100	50	18529	680
5	1793	897	66.024	29.79	1100	1050	50	16952	473
6	2344	1172	66.008	29.786	1050	1000	50	14883	317
7	4101	2051	65.978	29.798	1000	950	50	11661	142
8	9318	4659	65.934	29.79	950	918	32	8106	28
Basin 4 Stream 3									
1	808	404	66.054	29.769	1250	1200	50	13651	845
2	1292	646	66.045	29.766	1200	1150	50	12601	488
3	1551	776	66.033	29.767	1150	1100	50	11180	360
4	886	443	66.023	29.744	1100	1071	29	9961	326
Basin 5 Stream 1									
1	823	412	66.05	29.756	1250	1200	50	8369	508
2	838	419	66.043	29.756	1200	1150	50	7538	450
3	1525	763	66.033	29.757	1150	1100	50	6357	208
4	1538	769	66.019	29.757	1100	1050	50	4825	157
5	1964	982	66.003	29.755	1050	1000	50	3074	78
6	1946	973	65.985	29.756	1000	960	40	1119	23
Basin 5 Stream 2									
1	570	285	66.049	29.742	1232	1200	32	4412	248
2	1330	665	66.043	29.748	1200	1150	50	3462	130
3	966	483	66.033	29.745	1150	1100	50	2314	120
4	1704	852	66.021	29.741	1100	1050	50	979	29
Basin 5 Stream 2B									
1	1256	628	66.039	29.728	1200	1150	50	11918	474
2	1272	636	66.033	29.737	1150	1100	50	10654	419
3	1322	661	66.021	29.739	1100	1050	50	9357	354
4	1876	938	66.008	29.734	1050	1000	50	7758	207
5	3461	1731	65.985	29.726	1000	950	50	5090	74
Basin 5 Stream 3									
1	931	466	66.042	29.721	1200	1150	50	17760	954
2	1660	830	66.033	29.726	1150	1100	50	16464	496
3	1192	596	66.022	29.728	1100	1050	50	15038	631